Design and Analysis of a Bladeless Drone

A Final Year Project Report

Presented to

SCHOOL OF MECHANICAL & MANUFACTURING ENGINEERING

Department of Mechanical Engineering

NUST

ISLAMABAD, PAKISTAN

In Partial Fulfillment
of the Requirements for the Degree of
Bachelor of Mechanical Engineering

by

Saad Ejaz
Muhammad Shahzad

June 2021

EXAMINATION COMMITTEE

We hereby recommend that the final year project report prepared under our supervision by:

SAAD EJAZ	229739
MUHAMMAD SHAHZAD	217538

Titled: "DESIGN AND ANALYSIS OF A BLADELESS DRONE" be accepted in partial fulfillment of the requirements for the award of BACHELOR OF MECHANICAL ENGINEERING degree with grade ___

Supervisor: Dr. Muhammad Jawad Khan, Assistant Professor, Department of Robotics and Intelligent Machine Engineering, SMME	Dated:
Committee Member: Dr. Muhammad Safdar, Assistant Professor, Department of Mechanical Engineering, SMME	Dated:
Committee Member: Dr. Mian Ashfaq Ali, Assistant Professor, Department of Mechanical Engineering, SMME	Dated:

_____ _____

(Head of Department) (Date)

COUNTERSIGNED

Dated: _____ _____

(Dean / Principal)

ABSTRACT

With the rapid growth of the global drone market, drone safety has become a matter of prime importance. Among drone accidents, propeller-based injuries dominate both in the frequency of occurrence and the severity of the damage, making conventional drones unfeasible for indoor flights. The need for a design that is safe for indoor flights while retaining the utilities of a conventional multi-copter is rising. The proposed bladeless penta-copter consists of a central housing, inspired by the Coandă effect saucer, with four side arms radially extending from it. The side arms each utilize an air multiplier that allows the propulsion device to be concealed within the side arm, eliminating the exposure of bladed components with the surrounding. The geometry of the central housing along with the size of the air multiplier and the geometry of its airfoil is optimized using CFD analysis. The objective is to maximize thrust and minimize the weight of the drone structure and the aerodynamic drag it experiences. Following this, a plant model for the resulting design is developed using Simulink, with PID controllers tuned for 6 DOF control. The control simulations revealed satisfactory performance. Moreover, the optimization of geometric parameters resulted in a thrust-to-weight ratio of 1.5, and the energy losses owing to fluid flow within the air multiplier were acceptable. All of this coupled with the design's inherent safety features makes it a viable option for use cases demanding increased safety with a minor compromise to flight efficiency, such as the videography, monitoring, and surveillance of confined spaces and crowded areas.

ACKNOWLEDGMENTS

All praise to Allah Almighty who is the creator, maintainer, and regulator of the world. He is the one, who bestows and gives the power to us to think, utilize our expertise in knowledge in achieving remarkable solutions for mankind in every field of life. In the first place, therefore, we express our utmost thanks to Almighty Allah the omnipresent and creator of the worlds, who has endowed us with his blessings that enabled us to accomplish our work in the form of this project report. No words of thanks can be appropriate for His immense blessings.

We are also grateful to our loving and caring parents and siblings, who provided us full support through all possible resources with great patience throughout our project. We feel very lucky to have such parents. Without their confidence, we could not have reached our full potential.

We would like to express our sincere gratitude to our advisor Dr. Muhammad Jawad Khan for his worthy guidance and support throughout our project. His constant guidance helped us to tackle all the problems we faced during our research. We feel privileged to work under his supervision.

We are also thankful to the School of Mechanical and Manufacturing Engineering which provides us this opportunity to research in this developing and growing field. We are deeply grateful to our thesis committee members and faculty for their precious suggestions, support, and guidance throughout this project.

We are grateful to our friends, seniors, and class fellows for their moral support and help during this project.

ORIGINALITY REPORT

FYP-Bladeless Drone

ORIGINALITY REPORT

4%	3%	2%	2%
SIMILARITY INDEX	INTERNET SOURCES	PUBLICATIONS	STUDENT PAPERS

PRIMARY SOURCES

1	repository.udistrital.edu.co Internet Source	1%
2	harikrishnansuresh.github.io Internet Source	1%
3	bibliodigital.unijui.edu.br:8080 Internet Source	<1%
4	Submitted to University of Hertfordshire Student Paper	<1%
5	calhoun.nps.edu Internet Source	<1%
6	Submitted to Higher Education Commission Pakistan Student Paper	<1%
7	www.mathworks.com.au Internet Source	<1%
8	Submitted to University of Mauritius Student Paper	<1%
9	Rivas López, Santiago M., Mario R. Sobczyk S., Fabiano D. Wildner, and Eduardo A. Perondi.	<1%

TABLE OF CONTENTS

LIST OF TABLES

LIST OF FIGURES

ABBREVIATIONS

UAV	Unmanned Air Vehicle
EDF	Electric Ducted Fan
ESC	Electronic Speed Controller
ABS	Acrylonitrile Butadiene Styrene
FSA	Fan Swept Area
COG	Center of Gravity
FOS	Factor of Safety
PID	Proportional Integral Derivative
SLS	Selective Laser Sintering
FDM	Fused Deposition Modeling

NOMENCLATURE

Φ	Roll Angle
θ	Pitch Angle
ψ	Yaw Angle
ω_i	Rotational Speed for motor i
γ	Side Arm Tilt Angle
K_C	Thrust Constant for Central Fan
K_S	Thrust Constant for Side Fan
B_C	Torque Constant for Central Fan
B_S	Torque Constant for Side Fan
F_R	Resistive Force
F_D	Drag Force

CHAPTER 1: INTRODUCTION

The last few years have experienced substantial growth in the use of Unmanned Air Vehicles (UAV). UAVs of various sizes and configurations are being used for purposes spanning videography, monitoring, surveillance, humanitarian aid, sports, and research, among others. The drone market continues to grow and is projected to grow over 40 billion dollars by 2025 [1]. With such rapid growth in the usage of drones, special considerations need to be given to safe flights and minimal harm to life and property. This chapter describes in detail the safety risks associated with drone flights which motivate the need for a bladeless drone design.

1.1. Drone Safety Risks

Drone safety risks can be categorized into two types:

1. *Blunt force trauma* is caused by fast-moving drones. A substantial number of unmanned aircraft can fly at high speeds (some over 100 mph). Collision with such a vehicle can cause considerable bodily harm. Studies have manifested that a 500g drone flying at speeds in the range of 17 to 37 mph can generate forces ranging from 14 to 69 J, which can fracture the human skull [2].
2. *Cuts and piercing injuries* can be caused by high-speed propellers. Most drone propellers spin at speeds over 100 m/s which on collision can cause severe harm to sensitive areas of the body including the skin and the eyes. A case reported at an emergency department in the United States revealed that a nine-year-old male child went into a coma after a drone propeller was struck in his eye [3]. A similar trauma, for an adult man, was also documented [4]. The damage to the eyes and face, in this case, was severe.

This project only deals with improving safety for the second type of drone-related injury risks. Blunt force trauma is inevitable when an object with high momentum collides with parts of the human body at risk of injury. To reduce this, we can reduce the drone

momentum (mass and/or velocity) but that is not feasible as it will limit its functionality. Furthermore, such safety risks are not unique to flying vehicles and are altogether not considered.

On the other hand, the risk related to piercing injuries, caused by collision with sharp propellers, can be mitigated without compromising the utilities of the drone. Moreover, since propeller blades are long (to increase air flow), there is a significantly greater chance of collision with propeller blades than with other parts of a drone. Research conducted on injuries, seen in the emergency departments in the United States, caused by hobbyist aircraft and drones concluded that propeller injuries were the leading mechanism [5] for such injuries. This amounts to approximately 74.2% of all injuries caused by planes, helicopters, and drones, and 54.8% of all injuries caused by drones only. The research concluded with a need to focus on injury prevention methods related to drones.

Propeller blades cutting into delicate parts of the skin can be fatal, and while this alone justifies the need for a safer alternative, there are other reasons to consider. Not only are drone propellers harmful to humans, but they also pose a serious threat to other animals especially birds and pets. If we consider the loss of property, collision with propellers can easily destroy surrounding items susceptible to shear force. Moreover, propellers are a weak part of the drone and optimal propeller condition is essential to proper control. Damage to the propeller can cause loss of control which can lead to a crash. Not only does a crash entail monetary losses, but it can also harm people or animals in close vicinity.

Along with the nature of risks, we also need to consider the environmental factors associated with the risks. While these risks are notable in an open environment, they aggravate in the case of indoor flights. Proximity to humans and objects (as part of an indoor environment) means a greater chance of collision and harm (both bodily and monetary). This is also true for crowded environments. A crowd, in this case, can be defined in two ways: as a congregation of people or the use of multiple drones (swarm robotics) for performing complex tasks. With more drones, interacting with each other, a single propeller accident can lead to breakage followed by loss of control. In the worst

case, the collisions can propagate to other drones which can be disastrous. Furthermore, current research in human-drone interaction ([6] explores such interactions) has safety measures in place that limit the distance between the interacting human and the drone. The comfortable distance for small, unmanned air vehicles has been researched in [7] (albeit with inconclusive results). There is a strong possibility that such safety measures overall deteriorate the quality of interaction and the overall experience.

Additionally, drone regulations and bans relating to outdoor flights (for example, the drone ban in Punjab in 2019 [8]) can prompt drone users to shift indoors which unfortunately is a safety risk if conventional propeller blades are used. In the study [5] of drone injuries discussed before, 65.0% of all injuries caused by drones were caused at home. Altogether, a mechanism must be used to either replace or conceal sharp propeller blades for a safer drone design.

1.2. Project Objective

The project aims to study existing injury prevention mechanisms in drones (guards, air multipliers especially), and then propose a drone design that is considerably safer than conventional drones. The objective is to improve indoor flight safety while maintaining all the advantages of a conventional drone i.e., controllability, scalability, and payload capacity. Doing so will allow ease of use in videography, surveillance, and monitoring of environments with either more people (e.g., crowded areas such as weddings, concerts, and riots) or more drones (e.g., swarm robotics and agricultural monitoring).

CHAPTER 2: LITERATURE REVIEW

The need for a safer drone design is significant. The injuries are seen over the past few years of growth in drone usage justify the requirement of a more *domestic* drone, that not only is safer in the environment but also opens up the possibility of flights in confined spaces (indoor flights). This chapter discusses three principles/concepts that make drones safer (drones based on the Coandă effect, drone propeller guards, and air multipliers). It then compares existing *safe* drone designs and proposes the most effective technology. Lastly, existing work related to the chosen technology is discussed.

2.1. Making Drones Safer

The techniques used to make drones safer can be divided into two categories:

1. Decreasing the number of bladed components. A lower number would mean a lower chance of contact with bladed components. Drones based on the Coandă effect tend to accomplish this.
2. Shielding bladed components can also prevent contact with them. This shielding can be done partially (using drone propeller guards) or fully (using air multipliers).

2.1.1. Coandă Effect and the Flying Saucer

The ability of fluid emerging from an opening to stay attached to a convex surface is known as the Coandă effect [9]. The use of this effect for thrust generation in flying machines is as old as the discovery of this effect by Henri Coandă [10]. The mechanism involved the flow of fluid through an orifice and out towards a curved surface. Since the fluid stuck to the boundary of the surface, one could potentially vectorize this airflow to generate thrust for a body. Another significant result of this effect is entrainment i.e., drawing more air (secondary flow) from the surrounding, which could be the basis for additional thrust. Figure 1 shows and explains this effect in detail.

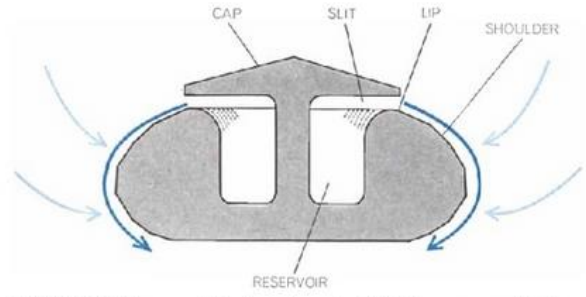

COANDA EFFECT was named for the tendency of a fluid, either gaseous or liquid, to cling to a surface that is near an orifice from which the fluid emerges. In this representation air from the reservoir emerges through the slit and, as shown by the dark color, closely follows the sides of the vessel. An important part of the effect is the tendency of the primary flow of air to entrain, or draw in, more air *(light color)* from the environment.

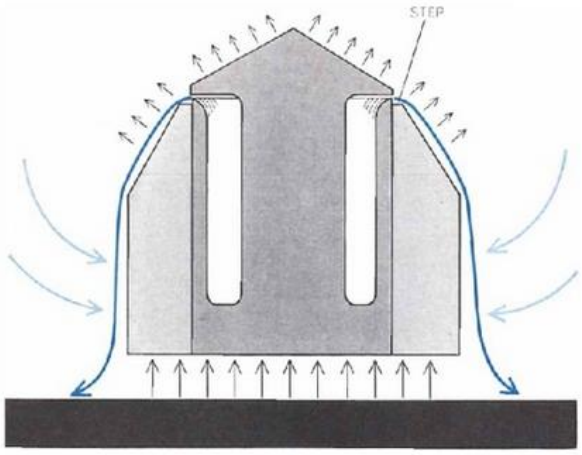

EXTERNAL NOZZLE was designed by the author in early tests of the Coanda effect as a means of generating lift. Pressure over the upper portion proved to be less than atmospheric; hence a vehicle with the shape of such a nozzle could be lifted by low pressure at top and higher pressure at bottom. Step near slit proved to be crucial in maintaining good lift.

Figure 1: The Coandă Effect and Thrust Generation (taken from [10])

Optimizing thrust generation through the Coandă effect by numerical modeling novel propulsion systems [11] and improving Coandă geometry [12] are popular research areas. Modern unmanned aircraft employing the Coandă effect do so by using a *flying saucer* [13]. In such a design an impeller is attached to a dome-shaped body (made out of a lightweight material such as Styrofoam), and fins and/or flaps present on the body are used to control the drone. Flaps are controlled using servo motors and allow for control in the lateral directions. Fins are used to counter yaw torque that is initially uncoupled because of the presence of a single motor. Moreover, the shape of the drone body is designed in a way that it vectorizes airflow in the vertical direction and also prevents flow separation. Figure 2 shows a detailed diagram of the flying saucer and its operating principles.

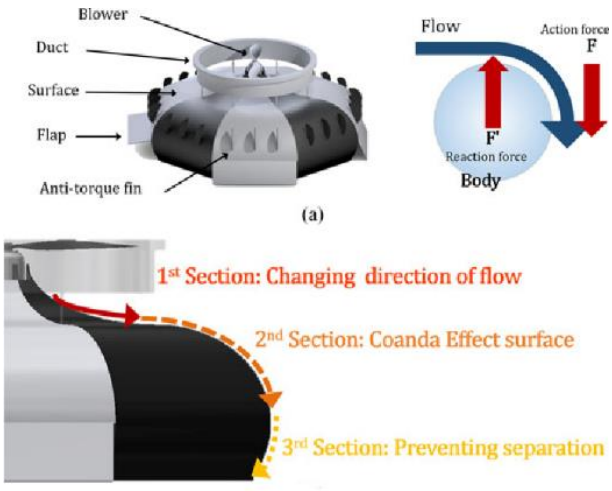

Figure 2: Working of a Flying Saucer (taken from [17])

Several designs employ similar principles, the most popular being the design by Geoff Hatton [14] who is believed to be the inventor of such a device (the device is also termed as a GFS – Geoff's flying saucer). Other designs have been fabricated that involve modification to the design parameters [15] and one that employs two motors with an elongated dome shape [16]. Numerical fluid modeling has also been conducted to optimize thrust generation and minimize resistive forces for such a shape [17] [18].

The use of the Coandă effect for thrust vectoring and novel control mechanisms (fins and flaps) have allowed for a usable drone design with just one bladed component. That and the fact that the bladed component is situated at a safer place (the span of the impeller is smaller than the span of the drone as a whole) as compared to propellers of conventional drones, has considerably mitigated the safety risks involved in UAVs. Additionally, the presence of guards around that single impeller further reduces the safety risks. However, it must be noted that because of the weak control mechanism, the drone body must be lightweight for this to work. This means that the drone is incapable of carrying significant payloads, which might be a huge disadvantage for many drone use cases. Moreover, environmental disturbances (wind, small objects, etc.) may adversely impact the drone because of its fragile structure. Nevertheless, such a drone is a good candidate for stealth operations [19] as it produces low noise and is lightweight.

2.1.2. Drone Propeller Guards

A propeller guard is a cage-like structure, usually made of a hard material, that surrounds the propeller. These guards either surround the propeller from the outer side only (image shown at the left in Figure 3) since it is the direction from which collision is most probable or from all sides (image shown at the right in Figure 3).

Drone guards such as these are effective and straightforward. They are easy to use and can be conveniently installed on a variety of drone designs. Moreover, several drone designs including [20] allow flights with or without the presence of guards. Users can then use their drone with guards until they are confident of their piloting skills. However, while these guards may seem the simplest solution, their use does have some disadvantages. Firstly, the partial guards do not limit exposure of propeller blades from all sides, and since such partial guards are the most commonly available guards, this is a safety risk. Moreover, all types of guards disrupt the airflow around propellers that are needed for optimal thrust, and this effect increases with an increase in the size of the guard and the area it covers. The meshes are shown in Figure 3 [21] also hinder proper airflow and can decrease propeller efficiency. Additionally, the guards add additional mass to the drone which coupled with a poor propeller efficiency can significantly decrease flight times.

Figure 3: Drone Propeller Guards - Partially (taken from [20]) and Fully (taken from [21]) Surrounded

Other minor disadvantages may include breakages which can either propagate to the propeller or make the drone unsteady, and unusual accidents in the case where the mesh-like structure of the guards may stick to objects in its surroundings (e.g., a tree branch). All of these reasons do not mean that drone guards should become obsolete, instead, they just indicate that there is room for improvement when it comes to safer drone flights.

2.1.3. Air Multipliers and the Bladeless Technology

An Air multiplier is a device that blows air out of a nozzle the shape of a ring. The vanes are hidden in their pedestal, and they direct the airflow through a toroid/loop. The driving motor and its bladed components are hidden in the tube that acts as the inlet to this toroid. The airflow out of the loop is a multitude of the airflow at the inlet by utilizing the principles of *entrainment, inducement,* and the *Coandă effect* (See Figure 4 and Figure 5). This device was first popularized by Dyson [22]. Dyson Fans use a mixed flow impeller to suck in air from vents and output airflow that is 15 times more than the inlet. The schematic diagram for such a system is shown in Figure 6.

This technology is referred to as bladeless technology, although it is not truly bladeless because of the presence of bladed components somewhere in the system.

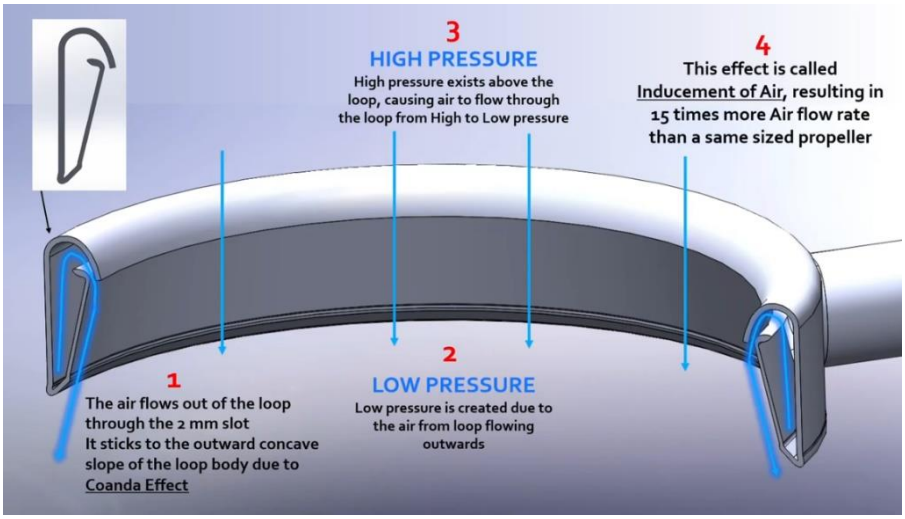

Figure 4: Air Multiplier – Inducement and the Coandă effect (taken from [23])

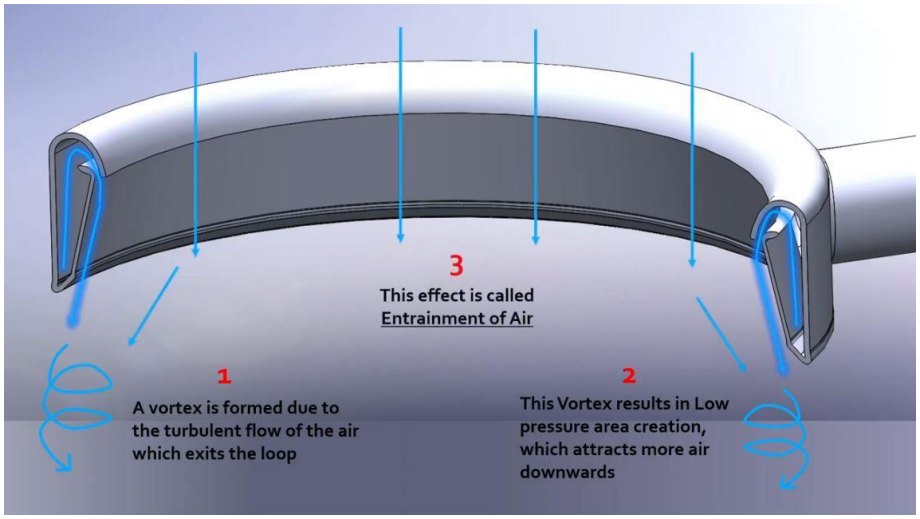

Figure 5: Air Multiplier - Entrainment (taken from [23])

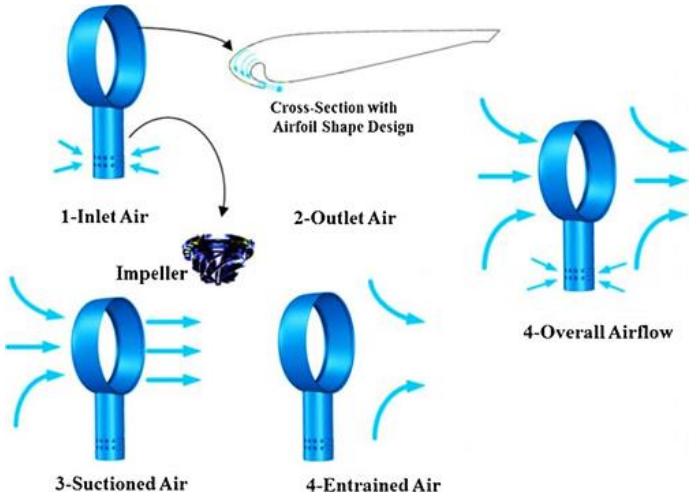

Figure 6: Bladeless Fan Schematic (taken from [24])

This technology has been tried in drones with little success. There are two different variants when it comes to bladeless drone designs. The first [25] employs a central propulsion device that blows air through tubes to a multitude of air multipliers (shown at the left in Figure 7). Control, in this case, is achieved by controlling the airflow to each air multiplier (for example, by using electronic valves). The second type of design defines the combination of a propulsion device and an air multiplier as a *bladeless thruster* [26] (shown

at the right in Figure 7). Control, in this case, is achieved similar to how it is achieved in a conventional drone, as each thruster is now independent.

The central propulsion drone has remained a concept design, while the one with bladeless thrusters was fabricated [27]. Control, in the case of bladeless thrusters, was modeled similar to how control would be modeled in a conventional quadcopter. However, the drone was unable to lift off because of insufficient pressure to create enough thrust.

Using bladeless technology ensures that bladed components of a drone remain concealed which allows for a considerably safer flight. However, this is countered by the additional mass that the air multiplier adds, and also the loss of energy owing to turbulent flow inside the air multiplier (although this might be offset to some extent by the thrust augmentation that an air multiplier provides owing to the principles of entrainment and inducement, as discussed before) and also the network of pipes that the drone must use for airflow. Because of this, the thrust generated may not be enough, as was seen in the case of [27].

Additionally, one can alter the shape and orientation of airfoil (defined as the cross-section of the toroid) to optimize thrust and minimize energy losses and mass. An air multiplier for drone technology thus needs to be purpose-built, in the sense that specifications and intuitions from airfoil optimized from fans (Dyson fan) may not transfer very well to drones. Therefore, such analyses are a part of this project.

Figure 7: Bladeless Drone with central propulsion (taken from [23]) and Independent Propulsion (taken from [27])

2.2. A Comparison of Existing *Safe* Drone Designs

This section list downs some of the major designs present in literature and also in the market, that directly or indirectly improve flight safety. It must be reiterated that drone safety can be increased by either reducing the number of bladed components or by enclosing them. Table 1 details the specifics of eight different designs and remarks on their feasibility. It must be noted that this table does not include *all* of the designs that may improve safety, but it does assure to some degree that all designs can fit as being similar to the principles behind one or more of the designs that are discussed.

Table 1: A comparison of relatively safer drones

Design name	Description	Propulsion System	Blade exposure	Fabrication of design	Feasibility of end product
Flying Saucer [13]	Dome-shaped body with an impeller on top or within to generate thrust using the Coandă effect.	1 with fins and flaps to achieve control	Depends on the positioning of the impeller	Yes	Mostly hovering capability. Limited translational movement.
Drone with no external propeller blades [25]	Central impeller forces air through four air multipliers.	1 central impeller. Control achieved using flow valves	Little to no blade exposure	Design patented. No fabrication.	-
Bladeless thrusters for autonomous multi-copters [27]	Propellers are replaced by a fan-air multiplier combo.	4 EDFs or centrifugal compressors	No blade exposure	Yes	Could not lift-off. Insufficient thrust

Herrera bladeless drone [28]	Three air multipliers with a central body with vents to suck in air.	3 or 1 (undetermined)	No blade exposure	No. Conceptual design only	-
ZeRone [29]	Helium blimp type drone with no bladed components.	24 micro-blowers, that provide thrust by ultrasonic vibration of piezo elements	No blades present	Yes	Slow response. Sensitive to inertial effects. Cannot handle payloads.
UNI-Copter [30]	Single motor drone with a spherical external structure that guards the propeller	Single BLDC with propeller	Some shielding from all sides	Yes	Takes up a large volume. Low payload capacity
Hover Camera Passport [31]	Quadrotor with foldable rectangular guards	Four BLDC with propellers	Some shielding from all sides	Yes. In market	Feasible other than the mass of complex drone guards
Gofleye [32]	Single motor drone with a camera on top, suitable for indoor use	Single BLDC with the drone body acting as a duct	Shielding from all sides	Yes	Feasible but with a low payload capacity

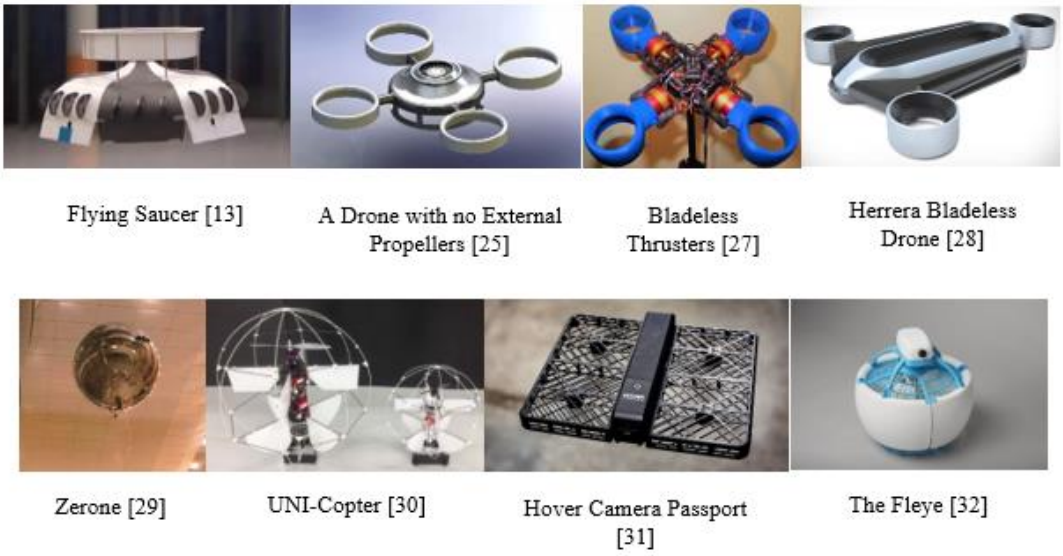

Figure 8: Images of the Drone Designs Listed in Table 1

Figure 8 is a collection of images of the drone designs listed in Table 1. The images are arranged according to the rows of Table 1, from top to bottom and left to right in Figure 8.

There are quite some designs that improve safety; however, apart from the designs employing different versions of the propeller guards (their disadvantages have been discussed in a previous section), there have been some serious drawbacks to replacing the *long-tested* conventional propeller-based drones. While some designs remain a concept [25] [28], others cannot carry enough payload due to either a weak propulsion system [29] or volume/stability/configuration issues [30] [32]. Some drone designs exist to serve unique purposes, such as the Fleye [32] and Hover Camera Passport [31] that excel at photography and videography, and the flying saucer [13] that can be effectively used for operations demanding stealth. These designs are without doubt shine in their utility but unfortunately cannot beat the versatility of conventional drones.

The closest to a conventional drone has been the use of bladeless thrusters [27] that maintain the control theory of conventional drones. However, the design fabricated had failed to provide sufficient thrust to lift its bulky body. This project aims to combine subtle

aspects from some of the mentioned designs to propose one design that is not situational and can replace everyday drones. The major focus would be given to the bladeless technology/air multipliers. The airfoil in consideration would be optimized to provide the highest thrust to weight ratio. Detail of existing work in improving air multiplier performance follows this section, which also identifies gaps in the research, upon which the methodology section is built.

2.3. Existing Work on Improving the Performance of Air Multipliers

Some research has been conducted regarding the effect of changing the specifications/dimensions of an air multiplier on its performance. The specifications include the dimensions of the airfoil as well as the diameter of the loop and its aspect ratio. The goal of the majority of this research was to improve performance of the air multiplier for use as a fan. Performance was judged by a discharge factor which was the ratio of the outlet volume flow rate through the fan (at some distance away from the fan, considering the fan is enclosed in a rectangular box as shown in Figure 9) to the inlet volume flow rate. Some consideration was also given to the sound levels produced. For numerical investigation, the air multiplier was enclosed in a rectangular fluid domain, as shown in Figure 9.

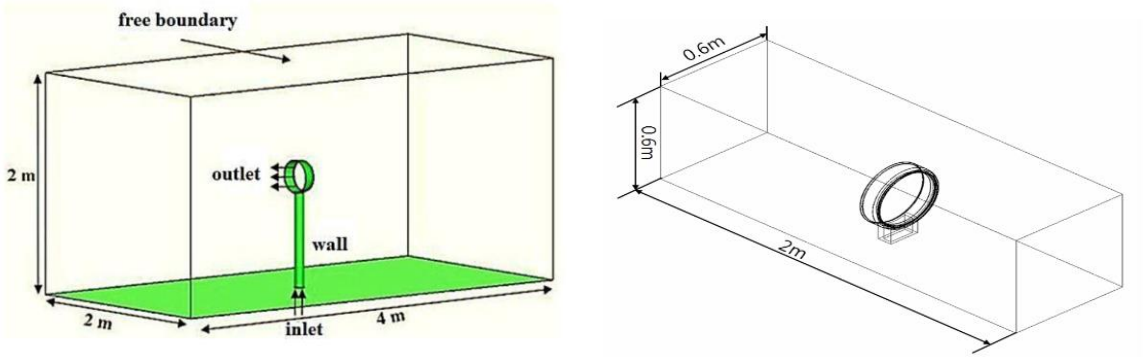

Figure 9: Example Fluid Domains for Air Multipliers (taken from [33] and [34])

The research in [33] used an air multiplier with a diameter of 30 cm, with a 473 Eppler airfoil profile in a setup shown at the left in Figure 9. The research concluded that the discharge ratio for such an air multiplier was 21 (higher if compared to the 15 that Dyson Fans have), and also established a linear relationship between the inlet and outlet mass flow rate. Moreover, acoustic performance was also judged, and it was concluded that increasing the inlet air flow (which in turn increased the outlet airflow) increases the noise level, and as such, there is a limit to the inlet airflow (inherent to a unique air multiplier) above which the noise produced is harmful to humans. This research was continued [35] for a 60cm bladeless fan (experimentally and numerically). The acoustic effects of the previous research were confirmed, and it was concluded that larger bladeless fans could be employed in industrial processes.

Another research [34] optimized four different parameters for maximum outlet flow rate for a given motor speed (analogous to inlet flow rate). The four parameters are shown in Figure 10. Three different values for each of the parameters, A, B, C, and D were considered for a total of nine different prototypes. These were numerically simulated on Ansys Fluent for outlet flow rate. The flow rate was maximum with A set to 1mm, B set to 17 degrees, C set to 4.2mm and D set to 10.8mm. The diameter of the air multiplier was set at 14 inches, and the outlet flow rate achieved through this configuration was 0.1693 kg/s.

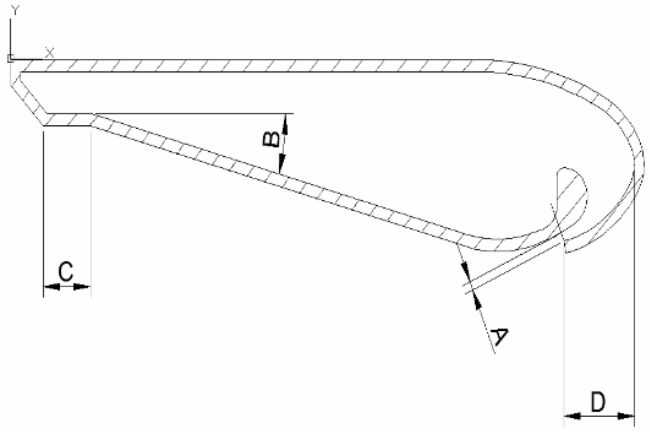

Figure 10: Airfoil Parameters for Optimization Considered in [34]

Another in-depth research [36] was carried out to evaluate the effect of changing geometric parameters on the performance of the fan. With reference to Figure 10, the parameters under consideration, in this case, were A and B and the height of the airfoil profile. The height is not shown in Figure 10. It is the length of the shorter side of the airfoil profile. Along with these parameters, the diameter of the air multiplier was also considered along with its aspect ratio (for both a circular and rectangular cross-section). Performance was based on discharge factor determined through numerical modeling, and it was concluded that a height of 3 cm was optimal (the width of all the prototypes was set to 10 cm), decreasing A increases the discharge factor, increasing the diameter of the air multiplier increases the discharge factor, a circular cross-section performed better than a rectangular cross-section, and that increasing the aspect ratio from 1 decreased the discharge factor considerably.

The bladeless thrusters research [27] took a different approach to measure the performance of a specific airfoil profile. This was based on the turbulency of flow. A turbulent flow (correlated to high-speed flow) outside the air multiplier was preferred to the formation of turbulent flow within the air multiplier.

To conclude, all of the research discussed in this section revealed that airflow through a bladeless fan is increased by a large factor and that this factor is unique to some of the important dimensions associated with the bladeless fan. However, it must be noted that for all of the research articles discussed, the performance metric was either the discharge factor or the noise level, which although are extremely important for a household fan but do not entirely guarantee the performance of such a device for a drone. Thrust/lift is the deciding factor in that case and while increased mass flow rate can indirectly mean increased thrust, it only does so if the flow rate in consideration is through the thrust-producing nozzle. For the mass flow discussed in the before-mentioned research, it can be categorized through two major sources: the first is the airfoil nozzle whose dimension is A (as in Figure 10) and the second is the space between the loop through which inducement and entrainment occur. A lift study is necessary to optimize the geometry of the airfoil profile for maximum thrust

for a bladeless drone. Moreover, the effect of diameter needs to be studied more carefully for a drone because while increasing diameter increases discharge factor (as [35] confirmed), it does also mean that the velocity profile throughout the loop gets more uneven, which can be troublesome when designing the control. This effect can be illustrated in a velocity contour diagram (across symmetry plane/s) of a bladeless fan with a considerable diameter, shown in Figure 11. With increasing diameter, the difference between the exhaust velocity at the cross-section closest to intake and the exhaust velocity at the cross-section farthest from the intake, increases which means that the lift generated is not always at a fixed point somewhere in the middle of the loop, as one would consider when modeling the system.

As one can notice, the airfoil shown at the left side of the contour diagram exhibits an air of very low velocity when compared with the one shown at the right. Since for a drone, intake airflow to the air multiplier would continuously vary, this can provide uneven thrust output with a higher response time (because of the large diameter). Therefore, this project while considering the advantageous effect of a larger air multiplier also considers controllability. In the next chapter, a drone consisting of air multipliers is designed and diameter along with other parameters are optimized for maximum thrust. Following that a control system is modeled and simulated.

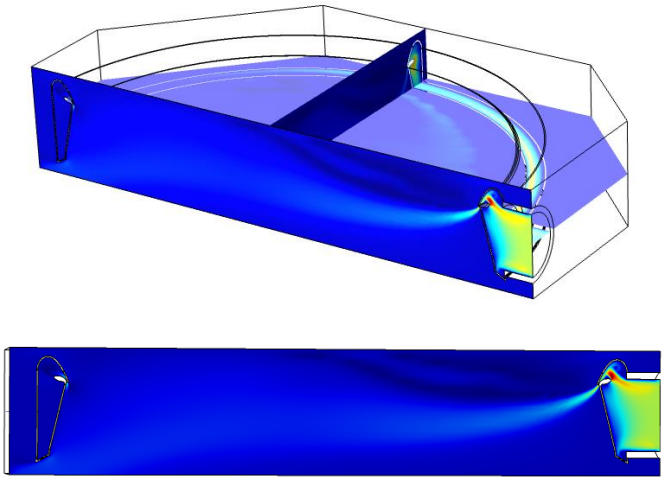

Figure 11: Velocity Contours at Central Planes of an Air Multiplier

CHAPTER 3: METHODOLOGY

The previous chapter explored several existing drone models (mostly in the research literature) that improve flight safety by either shielding bladed components or reducing their number. However, it can be noted that each design has drawbacks that do not allow it to replace the *long-tested* conventional drones. For example, the *flying saucer* [13] utilizes a single motor that vectorizes airflow over a dome (the Coandă effect) leading to less aerodynamic drag and a safer drone flight. However, the flying saucer cannot effectively replace a conventional drone as it has limited translational capabilities and cannot carry payloads. Moreover, the bladeless thrusters (defined as a combination of an air multiplier and an EDF) researched in [27] were promising. The design based on these thrusters utilized four air multipliers (as a replacement for propellers) in the same configuration as a quadcopter, essentially simplifying the control problem. However, the drone could not take off owing to considerable losses in the bladeless thrusters.

The design we propose is a penta-copter that takes inspiration from the subtle features of the design explained in the previous chapter. This design is aimed at providing more safety (especially for indoor flights) while retaining drone characteristics that make them useful (payload capacity, controllability, navigation, etc.) and lucrative. The following design methodology is discussed in detail in the upcoming sections:

1. An initial 3D design of the penta-copter is modeled.
2. Several parameters affecting either lift, drag or mass are identified.
3. These parameters are optimized sequentially.
4. After optimizing all parameters, the design is updated to reflect changes.
5. Fluid flow analysis is conducted to validate the design and determine essential constants for control modeling.
6. Results obtained from the analysis are used to model the control system for the design.

3.1. Design Modelling

Figure 12 shows the design modeled using SolidWorks. The design consists of four thrusters/arms (each with an EDF) arranged like [27] but declined at an angle. To compensate for additional losses due to turbulent flow in the air multipliers, a dome-shaped central housing consisting of an additional EDF is used. Altogether, there are five EDFs, making it a penta-copter. The central EDF provides the majority of thrust for lift-off while the thruster fans provide force for control and lateral movements.

3.1.1. Design Components

The design can be divided into two major components:

1. Central Housing
2. Thrusters

Figure 12: Proposed Bladeless Penta-copter

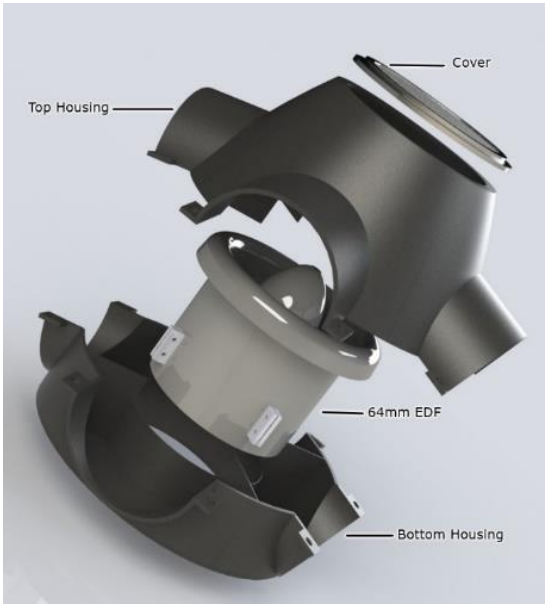

Figure 13: Exploded View of the Central Housing

The *central housing* (shown in Figure 13) consists of the central fan (which is responsible for take-off) and other electronics (controller, ESCs, etc. not shown in Figure 13). The central fan diameter can range from 60mm to 70mm. However, for analysis in this report, a 64mm ducted fan is proposed. This central housing provides additional thrust for lift-off and as such is proposed as a solution for the take-off problem concluded in [27]. Moreover, bladeless thrusters attach to the central housing through connectors. Additional payload and/or sensors can be compensated by attaching additional structures at the bottom of the housing. Furthermore, a cover may be installed at the top to provide additional protection against the blades of the central EDF.

The *thruster* (shown in Figure 14) consists of an air multiplier (Dyson Fan loop) and a thruster EDF (diameter ranging from 40mm to 50mm). The thruster assembly also contains *vents* for air intake into the fan. On top of each thruster, there is a compartment for a small battery. A 3S LiPo (1300mAh) battery is suitable for this purpose. All four of the batteries are connected in parallel. Placing the battery in such a configuration allows for symmetry, and thus does not affect the position of the COG.

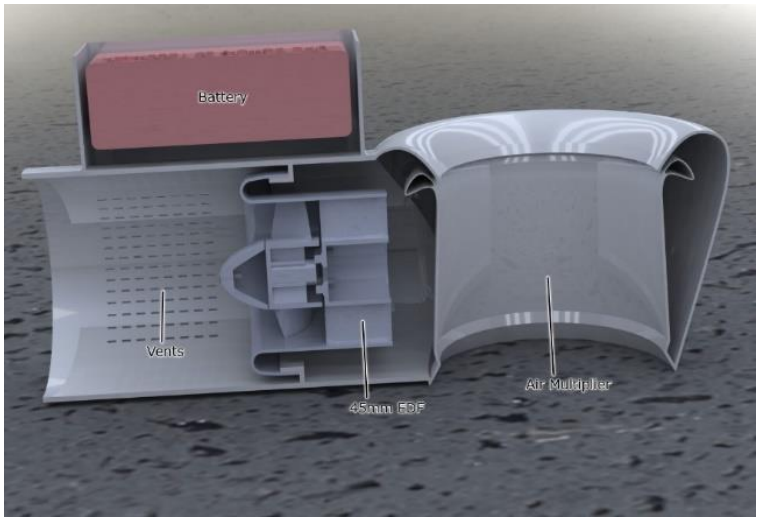

Figure 14: Cross-section View of the Thruster

Moreover, these thrusters are declined at a small angle (10-20 degrees). This slight adjustment is crucial as it allows for better controllability (will be discussed in later sections) on top of much-needed clearance and the possibility of dual-axis movement.

3.1.2. Material Selection

Owing to the complexity of the shapes involved in the design, almost all of the structure needs to be 3D printed. Therefore, ABS plastic is the preferred material. It is a commonly used, affordable 3D printing material and thus readily available. Moreover, its mechanical properties highly suit our design and are listed as follows:

1. Low density (1.07 g/cm^3) allows for a lower drone weight and hence higher surplus thrust.
2. High impact strength, high tensile strength, and resistance to environmental factors [36]. This means that the drone would be structurally sound.

However, owing to the high costs of printing using ABS plastic, Nylon may be a suitable alternative. This decision can only be made after considering production unit costing, after considering cheaper alternatives to the manufacturing process such as injection molding.

3.2. Fluid Flow Analysis

To validate this design, the total thrust provided by the five EDFs, τ, should exceed the sum of the weight of the design and the resistive forces it experiences:

$$\tau > mg + F_R$$

Here m is the mass of the drone and g is the gravitational field constant. $F_R$denotes the air drag in the vertical direction.

We cannot rely on the thrust values provided by the manufacturers for the thruster fans as the air flow is directed through an air multiplier, and additional losses and thrust augmentation due to inducement needs to be accounted for. A thrust factor (specific to air multiplier geometry) is to be determined and optimized. Moreover, the aerodynamic drag on the dome also needs to be determined and subsequently minimized.

For these purposes, the following CFD analyses are conducted. All simulations are performed using Ansys Fluent.

1. A preliminary thrust analysis for the central to validate values provided by the manufacturer and determine the difference.
2. Optimizing central dome aspect ratio by determining aerodynamic drag in the vertical and lateral direction.
3. Optimizing configuration and geometry of the airfoil of the air multiplier by determining the lift obtained.

3.2.1. Parameters for Analysis

From the above-mentioned analyses, the following four parameters are identified:

1. Central dome aspect ratio
2. Airfoil geometry
3. Airfoil tilt
4. Diameter of air multiplier

A detailed discussion on the setup of optimizing the above-mentioned parameters will follow.

3.2.2. Preliminary Fan Thrust Analysis

A 5-bladed 64mm fan was modeled using a rotating mesh (40,000 RPM). Figure 15 shows the geometry configuration. The unsteady simulation was run until convergence and the thrust produced were noted. The velocity streamlines for air movement around the fan are shown in Figure 16. This simulation was performed for the central EDF to determine lift coefficients that are to be used to validate the design and model its control. Since the central EDF directly interacts with the environment (without any involvement of air multipliers), such a simulation is enough to get fairly accurate results. The thrust value was found out to be 11.5 N. This value is close to the manufacturer values for the thrust of fans with similar inlet diameter and rotational speed.

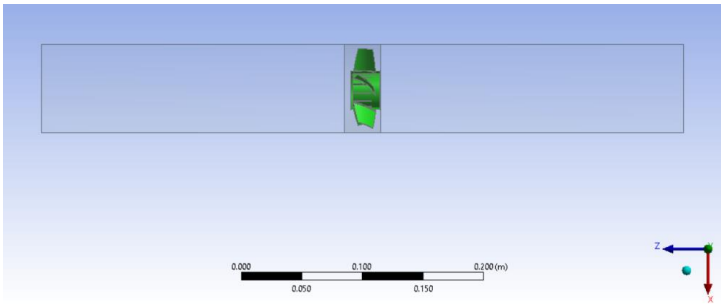

Figure 15: Geometry for Central EDF Simulation

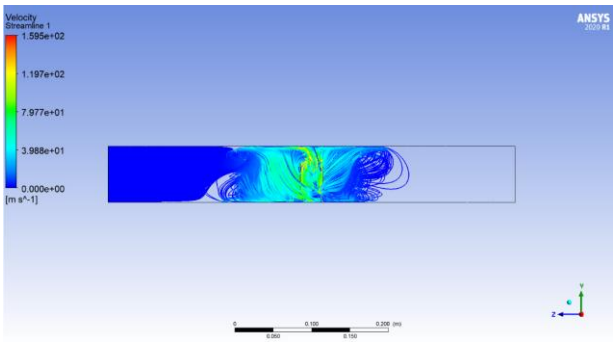

Figure 16: Velocity streamlines for Central Fan Thrust Simulation

3.2.3. Dome Aspect Ratio Optimization

The dome aspect ratio is defined as the ratio of the radius of the dome to its height. For this simulation, six different designs for the central dome were modeled, each with a different aspect ratio. Figure 6 shows two different models. The picture on the left in Figure 17 is a dome with a low aspect ratio and vice versa.

For each of these designs, an enclosure around the structure is generated. The length (x), width (y), and height (h) of this enclosure are set to be 0.375m, 0.260m, and 0.275m, respectively. Figure 18 shows such an enclosure. Subsequently, for each model, two simulations are run. The first simulation is run for aerodynamic drag for vertical movement of the drone. For this purpose, a velocity inlet of 5m/s is set at the top boundary, with the bottom boundary set as a pressure output with zero gauge pressure. All other boundaries are considered as walls. For the second simulation (for lateral movement), the left boundary is given a velocity inlet of 5m/s while the opposite boundary is set as a pressure outlet of zero gauge pressure. Similar to the first simulation, all other boundaries are set as walls. For both simulations, the flow is incompressible and the Spalart-Allmaras turbulent model is chosen. Drag force on the dome surface is determined for both the lateral and vertical movements. This data is tabulated respectively alongside the mass of each of the design variations to be optimized. The results are discussed in the next chapter.

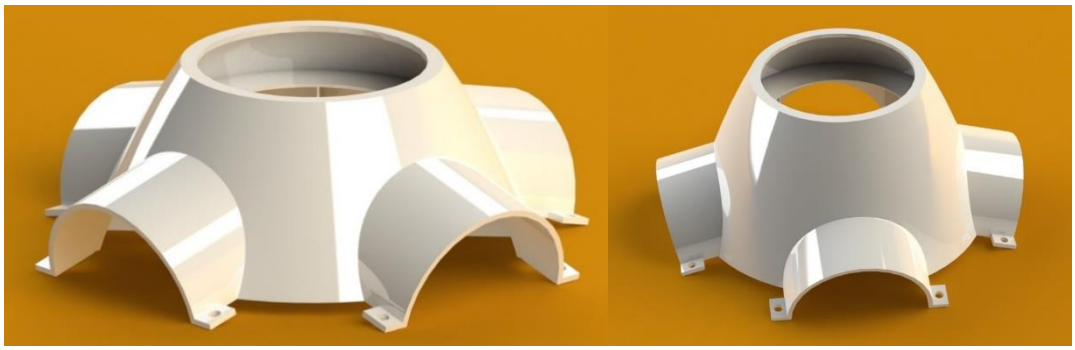

Figure 17: Dome Designs with Different Aspect Ratios

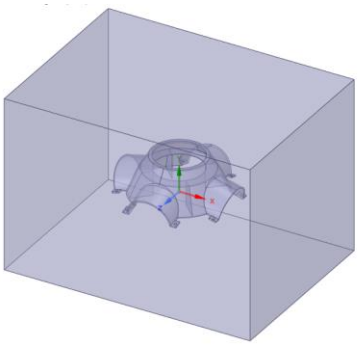

Figure 18: Example Dome Enclosure

3.2.4. Optimizing Air Multiplier Geometry and Configuration

In this section, the setup for optimization of three different parameters, namely the airfoil geometry, tilt, and diameter, is discussed.

Airfoil geometry in this regard is defined as the dimensions associated with the cross-section of an air multiplier. Airfoil geometry for an air multiplier has been optimized before (as discussed in Chapter 2), but these optimizations are limited to measurement of flow rate multiplication factor [35] and/or sound levels [33]. However, the numerical study in this report is targeted at optimizing the *thrust* achieved. Moreover, airfoil tilt is defined as the angle between the border-side of the airfoil with the vertical axis. This is demonstrated in Figure 8. The picture on the left in Figure 19 is an airfoil with a zero tilt angle, while the one on the left shows a tilt angle of 14 degrees.

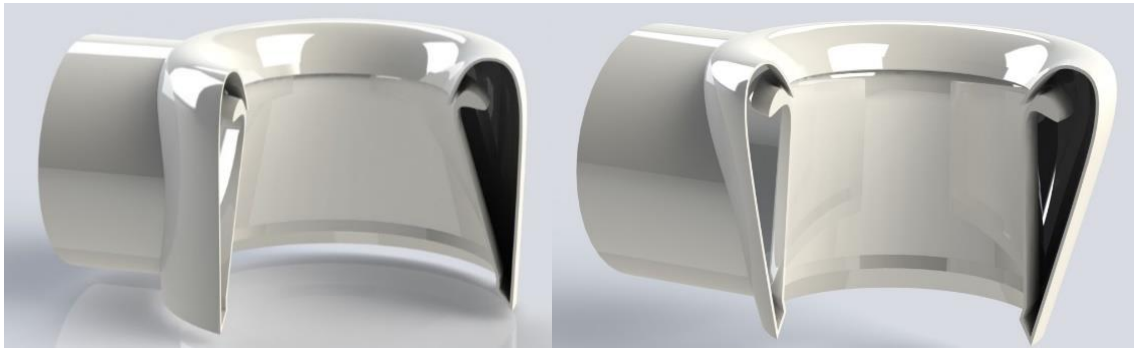

Figure 19: Air Multipliers with Different Airfoil Tilt Angles

Alongside the two tilt angles shown in Figure 19, two other tilt angles (7 degrees and 10 degrees) were also analyzed. For all four of these tilt angles, three different airfoil geometries (namely narrow, standard, wide) were analyzed. The differences between the prototypes are in the size of the nozzle, the width of the airfoil, and the angle of flow exhaust through the nozzle. Together, the three geometries (shown in Figure 20, all dimensions in mm) along with the four tilt angles account for *twelve different variations of the airfoil*. The diagrams in Figure 20 can be scaled according to drone specifications (for this project, the dimensions were scaled down).

For all twelve variations, an enclosure is set up with a significant cushion in the vertical direction. By doing so, we can determine the effect of air inducement on lift generation ─ a phenomenon also known as *thrust augmentation*. The cushion values for the enclosure are shown in Figure 21. It can be noted that the top and bottom cushion values (50mm) are significantly greater than the remaining cushion values. As a comparison, the height of the air multiplier is 64.76mm (scaled down from 104.83mm from the prototype diagrams), making the vertical cushion to be approximately 77% on each side. This ensures that the effect of inducement for enhanced thrust is considered in the simulations.

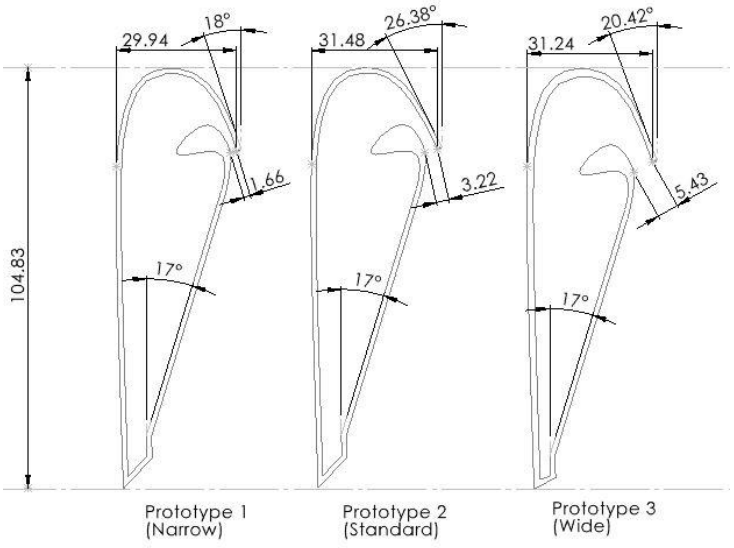

Figure 20: Three Different Types of Airfoil Geometries

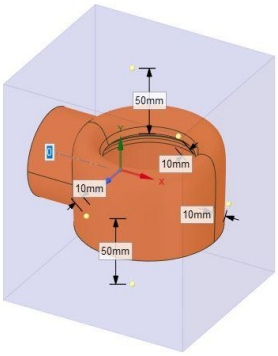

Figure 21: Cushion Values for Thruster Enclosure

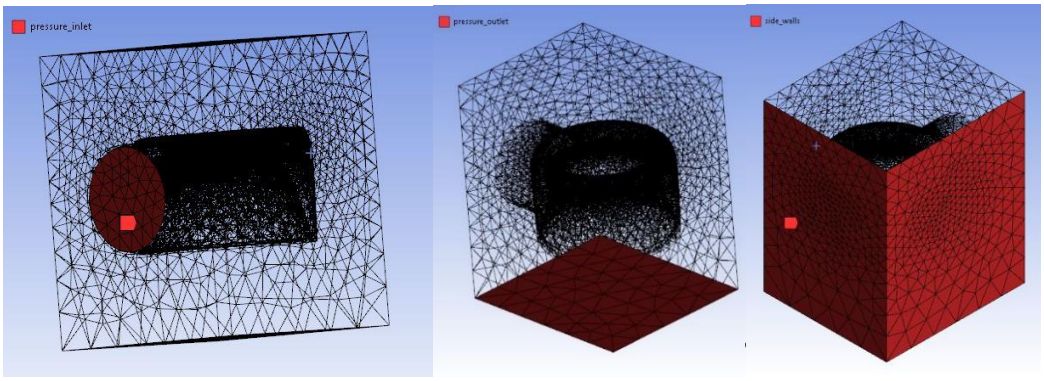

Figure 22: Thruster Enclosure Mesh with Boundary Conditions

The boundary conditions comprise a pressure inlet and two pressure outlets (top and bottom boundary, with reverse flow expected at the top and also tabulated). A pressure inlet is favored over a velocity inlet because the compressible flow is further entrained at the nozzle, which may decrease the velocity at the inlet (which otherwise a velocity inlet boundary condition will enforce). The side faces (left, right, front, and back along with the air multiplier faces are set as walls). Figure 22 shows the mesh alongside boundary conditions (not all faces shown).

For the total and static pressure at the inlet, flow properties at the exhaust of the Hyperflow 56mm (housing diameter, the actual fan diameter is approximately 47.2mm) ducted fan with a Brushless 24-45-3790 (GPMG5185) running with 3S LiPo cells is considered. Although this EDF model may be difficult to find in the market, the data and calculations

found in the datasheet [37] allow for adequate analysis. Static pressure (gauge) at the inlet of the air multiplier (leading off of the exhaust of the fan) is a sum of the pressure jump across the fan (assuming that pressure at fan inlet is atmospheric, this value is taken from calculations from [38] and is approximately 1.78 kPa for a 90% FSA exhaust) and the pressure increase due to difference in the diameter of the air multiplier inlet and exhaust of 90% FSA. The latter pressure increase can be found using the Bernoulli Equation shown below.

$$\rho \frac{v_i^2}{2} + \rho g z_i + p_i = const$$

This value is found out to be 1.16 kPa making the static pressure (gauge) at the air multiplier inlet to be 2.94 kPa. Fan exhaust velocity is determined from [37] and using that the air multiplier inlet velocity is calculated by using the conservation of mass. This is then used to determine total pressure (stagnation pressure) using the Bernoulli equation shown above (since at this point the flow is incompressible with very low velocity). The stagnation pressure (gauge) comes out to be 3.51 kPa. To summarize, the static pressure at the pressure inlet is 2.94 kPa while the total pressure is 3.51 kPa. Combined with zero gauge pressure at the outlet, the compressible flow simulation (for each of the four airfoil variations) is run using the Spalart-Allmaras model until convergence. Two findings are of prime importance:

1. The lift force acting on the air multiplier. This determines the thrust one thruster can provide and can be used to model losses.
2. The maximum velocity at two diametrically opposite points in the nozzle. This can be used as a measure of the unevenness of the fluid flow along the air multiplier loop.

Furthermore, one of these variations (wide/Prototype 3 + zero tilt angle) is used to optimize the air multiplier diameter. Six different designs were simulated, each with a different diameter, ranging from 40mm to 100mm. These simulations were similar to the simulations for the airfoil geometry with regards to setup, meshing, and boundary conditions.

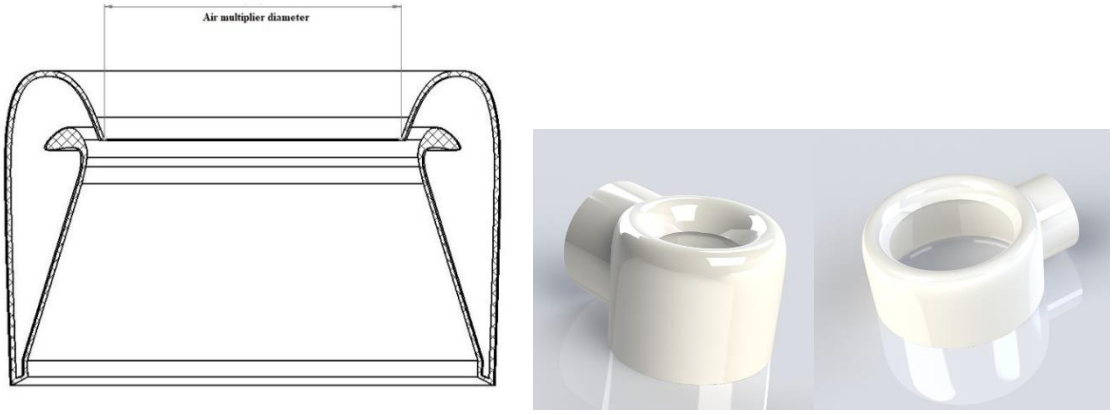

Figure 23: Air Multiplier Diameter - Definition and Examples

Figure 23 defines the air multiplier diameter and also shows two variations of the design with different diameters. The image on the right of Figure 23 is an air multiplier with a large diameter (approximately 92mm) while the image in the center of Figure 23 is an air multiplier with a small diameter (approximately 43mm).

The results of these simulations are also tabulated and discussed in further chapters.

3.3. Control Modelling

One advantage of using a design such as this is the ease of controllability that arises from similarities with a conventional quadrotor. The proposed penta-copter, similar to a quadrotor, is an underactuated system. Out of the six DOF, only four degrees of freedom are directly controlled (translation in the vertical axis along with three rotational movements i.e., movement in z-axis and roll, pitch, yaw), while the rest (lateral translations i.e., movement in the x and y axes) are achieved by first tilting the penta-copter (roll angle for movement in the direction of y-axis, and pitch angle for movement in the direction of y-axis). Figure 24 shows the control architecture of such a system. The controllers used in this case are either PD or PID controllers.

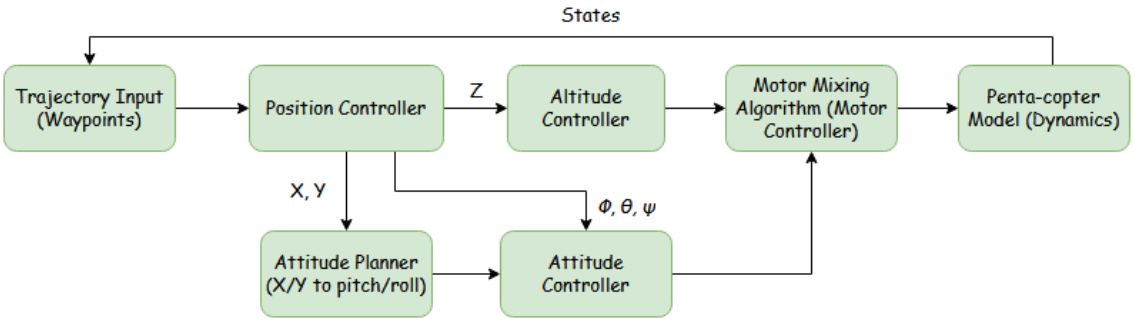

Figure 24: Penta-copter Control Architecture

For the sake of simplicity, environmental effects and sensor feedback are not considered in the control simulation of the penta-copter in this project. Furthermore, this section is further divided into sections describing plant model equations for the penta-copter, setting the motor mixing algorithm, and introducing the setup for control simulation on Simulink.

3.3.1. Penta-copter Plant Model

It must be noted that the penta-copter model proposed in this report (refer to Figure 12) has a rotor orientation that is different from that of a conventional quadrotor. Rotors in the proposed design have their rotation axes aligned perpendicular to the rotation axis of the central rotor. Therefore, the uncoupled yawing moment of the central motor cannot be countered with the side rotors. For this reason, the tilt (at an angle of γ, shown in Figure 25) of the side arms is essential. Tilting the side arms at a small angle provides a portion of the motor moment in the yaw direction.

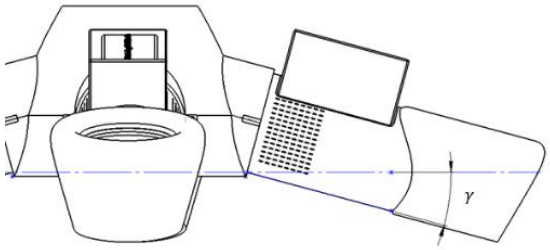

Figure 25: Thruster Tilt Angle Defined

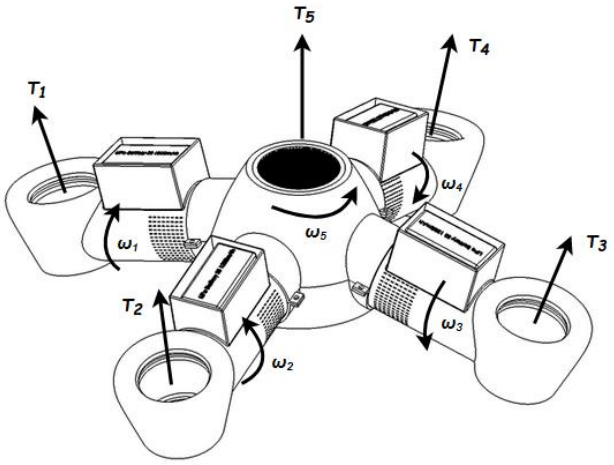

Figure 26: Bladeless Penta-copter Motor Thrust and Rotation Direction

All four side rotors collectively produce a yaw moment to counter the uncoupled yaw of the central rotor. Figure 26 shows the thrust produced by each of the five fans and their rotation configuration. The side fans are selected to be clockwise rotating fans while the central fan is a counter-clockwise fan.

The plant model equations derived in this section are an extension of the quadcopter plant model derived in [40]. The model is described using two frames of reference: inertial frame {O} (with gravity acting in the negative vertical direction) and a body-fixed frame {B}. For the inertial frame, the position of the COG of the penta-copter is defined by $X, Y, and\ Z$, while the angular position (attitude) is defined by Φ (roll), θ (pitch), and ψ (yaw). The translational velocities ($V_x, V_y, and\ V_z$) and rotational velocities ($P, Q, and\ R$) are defined in the body frame. Moreover, the orthogonal rotation matrix from {B} to {O} is defined as:

$$R_{\blacksquare} = \begin{bmatrix} C_\Psi C_\theta & C_\Psi S_\theta S_\Phi - S_\Psi C_\Phi & C_\Psi S_\theta C_\Phi + S_\Psi S_\Phi \\ S_\Psi C_\theta & S_\Psi S_\theta S_\Phi + C_\Psi C_\Phi & S_\Psi S_\theta C_\Phi - C_\Psi S_\Phi \\ -S_\theta & C_\theta S_\Phi & C_\theta C_\Phi \end{bmatrix}$$

where $C_\theta = cos(\theta)$ and $S_\theta = sin(\theta)$. For each motor, let T be the thrust it produces. Through a lumped parameter approach, it is known that the thrust is proportional to the square of the rotational speed, such that:

$$T = K_i \omega_i^2$$

where $K_i = K_s$ for $i \in \{1, 2, 3, 4\}$, and is defined as the thrust constant for side motors, while $K_5 = K_c$ which is defined as the thrust constant for the central motors. The values of these constants are determined after thrust values (post-optimization) are determined for each propulsion unit.

Similarly, the torque produced by a motor can be considered proportional to the square of the rotational speed (if we ignore the effect of the derivative of this rotational speed), such that:

$$\tau = B_i \omega_i^2$$

where B_s and B_c are defined similarly to how K_s and K_c are defined. For simplification purposes, this value is taken the same for both side and central fans.

Using these equations and the configuration described in Figure 27, we can calculate the forces in three translational directions and moments in the three rotational directions as follows (l is the distance from the COG to the center of an air multiplier):

$$\begin{bmatrix} T_x \\ T_y \\ T_z \\ m_\Phi \\ m_\theta \\ m_\varphi \end{bmatrix} = \begin{bmatrix} -K_s \sin\gamma & 0 & K_s \sin\gamma & 0 & 0 \\ 0 & K_s \sin\gamma & 0 & -K_s \sin\gamma & 0 \\ K_s \cos\gamma & K_s \cos\gamma & K_s \cos\gamma & K_s \cos\gamma & K_c \\ -B_s \cos\gamma & K_s l & B_s \cos\gamma & -K_s l & 0 \\ -K_s l & -B_s \cos\gamma & K_s l & B_s \cos\gamma & 0 \\ B_s \sin\gamma & B_s \sin\gamma & B_s \sin\gamma & B_s \sin\gamma & -B_c \end{bmatrix} \begin{bmatrix} {\omega_1}^2 \\ {\omega_2}^2 \\ {\omega_3}^2 \\ {\omega_4}^2 \\ {\omega_5}^2 \end{bmatrix}$$

Setting the net thrust acting on the penta-copter as F_B and the drag as F_D, we have:

$$F_B = \begin{bmatrix} T_x \\ T_y \\ T_z \end{bmatrix}$$

$$F_D = \begin{bmatrix} A_x & 0 & 0 \\ 0 & A_y & 0 \\ 0 & 0 & A_z \end{bmatrix} \begin{bmatrix} \dot{X} \\ \dot{Y} \\ \dot{Z} \end{bmatrix}$$

The equation of motion becomes (gravity as the only external force):

$$\begin{bmatrix}\ddot{X}\\ \ddot{Y}\\ \ddot{Z}\end{bmatrix} = \begin{bmatrix}0\\ 0\\ g\end{bmatrix} + R_{\blacksquare}\frac{F_B}{m} - \frac{F_D}{m}$$

which after the substitution shown below resolves to:

$$\begin{bmatrix}\dot{X}\\ \dot{Y}\\ \dot{Z}\end{bmatrix} = \begin{bmatrix}U\\ V\\ W\end{bmatrix}$$

$$\dot{U} = (cos\,\psi\, cos\,\theta)\frac{T_x}{m} + (cos\,\psi\, sin\,\theta\, sin\,\Phi - sin\,\psi\, cos\,\Phi)\frac{T_y}{m} + (cos\,\psi\, sin\,\theta\, cos\,\Phi + sin\,\psi\, sin\,\Phi)\frac{T_z}{m} - \frac{A_x U}{m}$$

$$\dot{V} = (sin\,\psi\, cos\,\theta)\frac{T_x}{m} + (sin\,\psi\, sin\,\theta\, sin\,\Phi + cos\,\psi\, cos\,\Phi)\frac{T_y}{m} + (sin\,\psi\, sin\,\theta\, cos\,\Phi - cos\,\psi\, sin\,\Phi)\frac{T_z}{m} - \frac{A_y V}{m}$$

$$\dot{W} = -g - sin\,\theta\frac{T_x}{m} + sin\,\Phi\, cos\,\theta\frac{T_y}{m} + cos\,\theta\, cos\,\Phi\frac{T_z}{m} - \frac{A_z W}{m}$$

For rotational motion, we have:

$$M_B = \begin{bmatrix}m_\Phi\\ m_\theta\\ m_\varphi\end{bmatrix}$$

We also define a rotational drag as A_R, which is the constituent of M_D. The resulting equation of motion comes out to be:

$$\dot{v} = I^{-1}\left(-\begin{bmatrix}P\\ Q\\ R\end{bmatrix} \times \begin{bmatrix}I_{XX}P\\ I_{YY}Q\\ I_{ZZ}R\end{bmatrix} - I_R\begin{bmatrix}P\\ Q\\ R\end{bmatrix} \times \begin{bmatrix}rot_x\\ rot_y\\ rot_z\end{bmatrix} + M^B - M^D\right)$$

where I_R is the rotational inertia of each motor (for simplification purposes, this value is taken the same for both kinds of fans). Moreover, the rotations are defined as:

$$rot_x = \omega_1\, cos\,\gamma - \omega_3\, cos\,\gamma$$

$$rot_y = \omega_2\, cos\,\gamma - \omega_4\, cos\,\gamma$$

$$rot_z = (\omega_1 + \omega_2 + \omega_3 + \omega_4)\, sin\,\gamma - \omega_5$$

This resolves to:

$$\dot{P} = \frac{I_{XX} - I_{ZZ}}{I_{XX}}QR - \frac{I_R}{I_{XX}}\left(Q * rot_z - R * rot_y\right) + \frac{m_\Phi}{I_{XX}} - \frac{A_R P}{I_{XX}}$$

$$\dot{Q} = \frac{I_{zz} - I_{XX}}{I_{YY}} PR - \frac{I_R}{I_{YY}} (P * rot_z - R * rot_x) + \frac{m_\theta}{I_{YY}} - \frac{A_R Q}{I_{YY}}$$

$$\dot{R} = \frac{I_{XX} - I_{YY}}{I_{ZZ}} PQ - \frac{I_R}{I_{ZZ}} (P * rot_Y - Q * rot_x) + \frac{m_\psi}{I_{ZZ}} - \frac{A_R R}{I_{ZZ}}$$

Finally, the transformation from the body frame to inertial frame for rotation is given by:

$$\begin{bmatrix} \dot{\Phi} \\ \dot{\theta} \\ \dot{\psi} \end{bmatrix} = \begin{bmatrix} 1 & sin\,\Phi\, tan\,\theta & cos\,\Phi\, tan\,\theta \\ 0 & cos\,\Phi & -sin\,\Phi \\ 0 & \frac{sin\,\Phi}{cos\,\theta} & \frac{cos\,\Phi}{cos\,\theta} \end{bmatrix} \begin{bmatrix} P \\ Q \\ R \end{bmatrix}$$

These equations define the plant model which will be coded in a MATLAB level 2 S-function block (also an extension of code by [40], see Appendix I) with 5 motor speeds as input and 12 outputs ($X, Y, Z, U, V, W, P, Q, R, \Phi, \theta, \psi$), which define the system states and are also used as feedback.

3.3.2. The Motor Mixing Algorithm

For the motor mixing algorithm, since the system is underactuated, only four degrees of freedom will be independently controlled. For that purpose, the following equation is considered:

$$\begin{bmatrix} T_z \\ m_\Phi \\ m_\theta \\ m_\varphi \end{bmatrix} = \begin{bmatrix} K_s\, cos\,\gamma & K_s\, cos\,\gamma & K_s\, cos\,\gamma & K_s\, cos\,\gamma & K_c \\ -B_s\, cos\,\gamma & K_s l & B_s\, cos\,\gamma & -K_s l & 0 \\ -K_s l & -B_s\, cos\,\gamma & K_s l & B_s\, cos\,\gamma & 0 \\ B_s\, sin\,\gamma & B_s\, sin\,\gamma & B_s\, sin\,\gamma & B_s\, sin\,\gamma & -B_c \end{bmatrix} \begin{bmatrix} {\omega_1}^2 \\ {\omega_2}^2 \\ {\omega_3}^2 \\ {\omega_4}^2 \\ {\omega_5}^2 \end{bmatrix}$$

To determine motor speeds from the required four states, the 4x5 matrix needs to be inverted. However, the matrix is rank deficient with nullity equal to 1. The basis for this null space is $[-1,\ 1, -1,\ 1,\ 0]$. This means that the expression for ${\omega_5}^2$ would be constant, while we have a single degree of freedom for values for the rest of the rotations. For this project, the only goal was to keep the coefficient of T_Z same for ω_i for all $i \in \{1, 2, 3, 4\}$. This is necessary because, for the side motors, we need the same energy usage for all motors in the hover state. This makes sure that the wear level for all motors remains similar

for obvious reasons. The resulting motor mixing algorithm is coded in a MATLAB function block with four states as input and five motor speeds as output. The output is then fed to the plant block described in the previous section. The complete motor mixing algorithm is shown in Appendix II.

3.3.3. Setup for Simulating Control

Following the configuration described in Figure 26, the plant model and the motor mixing algorithm were coded using Simulink in MATLAB. The plant model was a level-2 S function (see Appendix I), and the motor mixing algorithm was a simple MATLAB function (see Appendix II). Six PID controllers were used and PID constants were tuned. The results were simulated using the Simulink 3D Animation toolkit. Figure 27 shows the Simulink model and Figure 28 shows snapshots of the virtual environment.

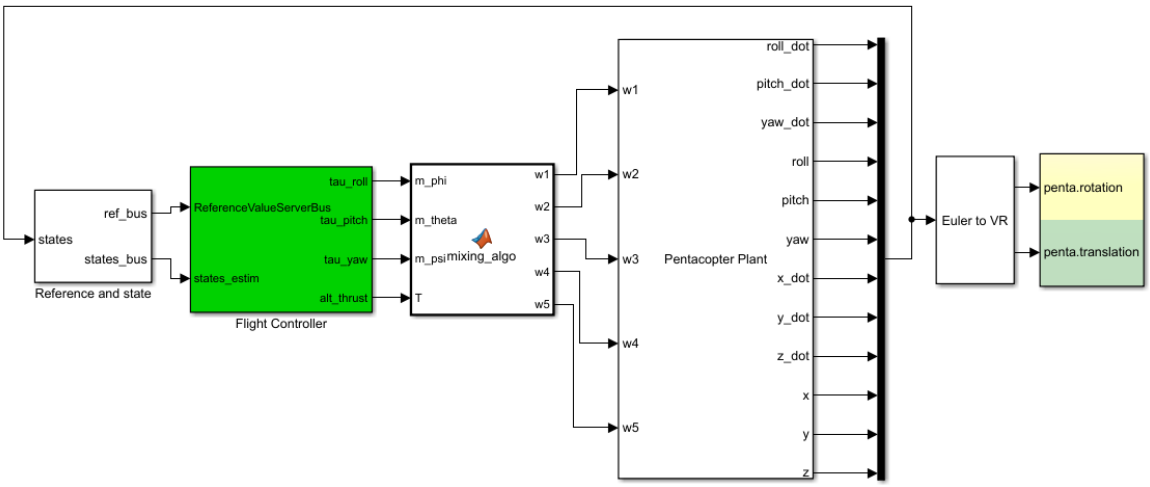

Figure 27: Simulink model for the Proposed Penta-copter

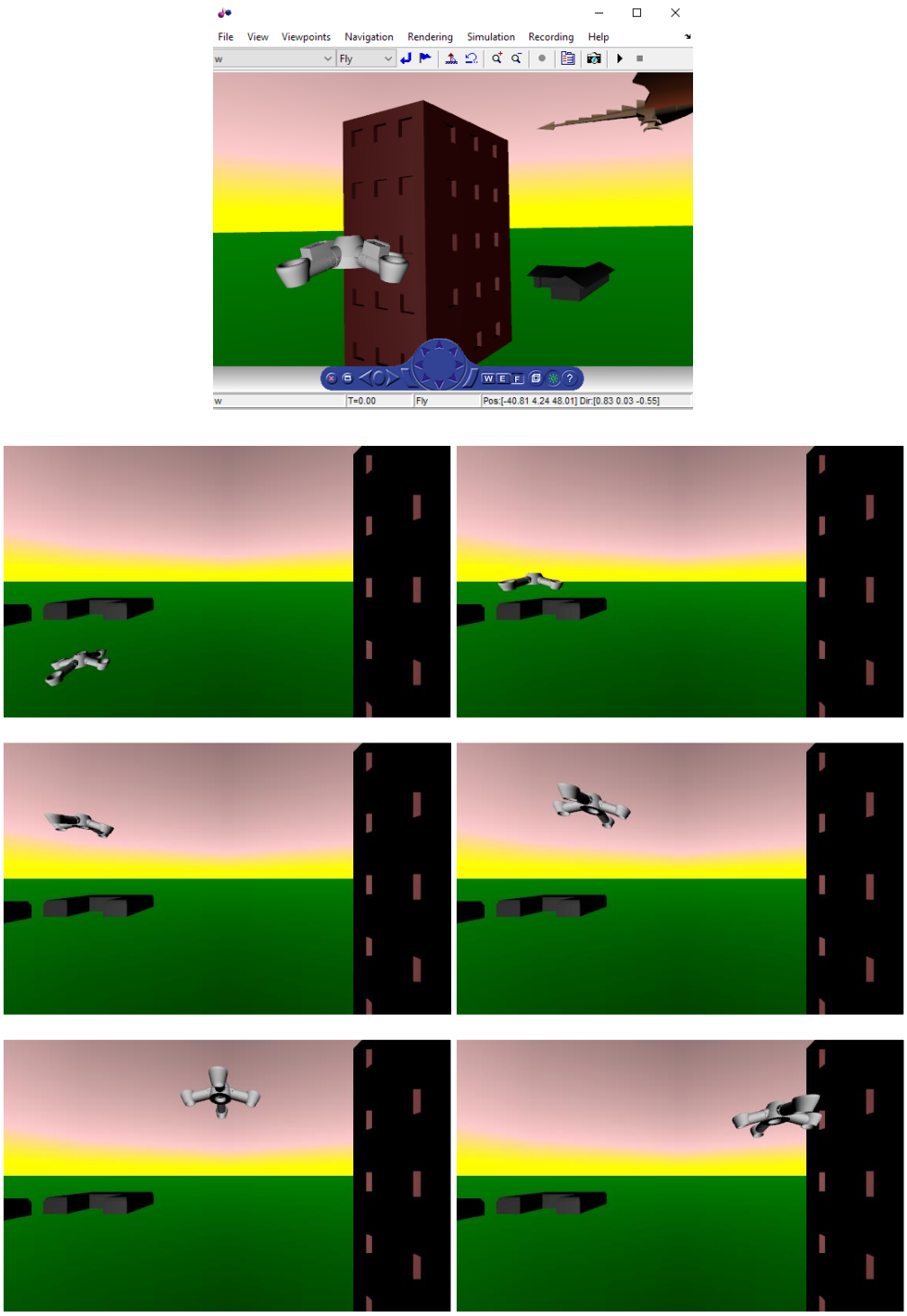

Figure 28: Snapshots of VR Environment for Drone Simulation

CHAPTER 4: RESULTS AND DISCUSSIONS

This chapter will focus on results from all of the simulations described in the previous chapter. Following that final parametric results would be selected, and their significance discussed. Using those parameters, the final design would be validated. A component list and costing are also included in this chapter.

4.1. Parametric Results

4.1.1. Dome Aspect Ratio

Aerodynamic drag analysis on central domes with various aspect ratios concluded with the following results. Figure 29 shows the velocity contours in the XY symmetry plane of an example central dome. The picture in the right of Figure 29 shows contours when the drone is traveling up at a speed of 5m/s, and the picture in the left of Figure 29 shows contours when the drone is traveling laterally at 5m/s. Moreover, it must be noted that while the drone moves laterally, it is inclined at some angle to the vertical axis (because the drone is underactuated and lateral translations are achieved by changing attitude). This is not considered in this simulation because of two reasons:

1. The contact area is similar for both cases.
2. All domes are simulated under the same conditions.

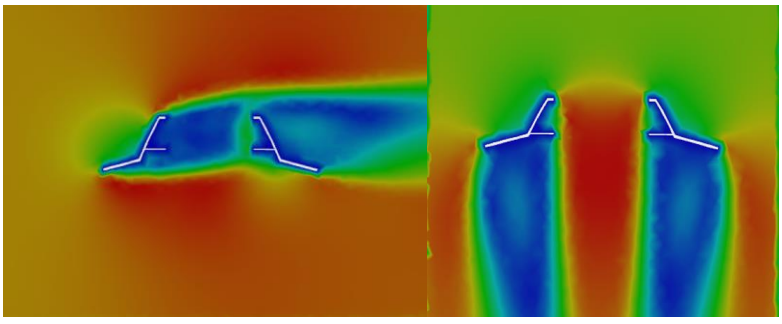

Figure 29: Velocity Contours for Drag Simulation of Central Dome

For each dome variation, three values were recorded: vertical drag, lateral drag, and mass of the dome. A single parameter (resultant force) was evaluated to judge performance. Table 2 shows these results:

Table 2: Recorded Data for Central Dome

Aspect Ratio	Vertical Drag (F_V) N	Lateral Drag (F_L) N	Mass (m) g	Resultant Force $(F_R = \sqrt{(F_V - mg)^2 + F_L^2})$ N
0.9333	0.371	0.163	71.69	1.087
0.9655	0.344	0.170	70.32	1.047
1.0000	0.345	0.166	68.99	1.035
1.0606	0.349	0.166	66.48	1.014
1.1666	0.357	0.153	63.64	0.993
1.2500	0.360	0.144	61.65	0.975

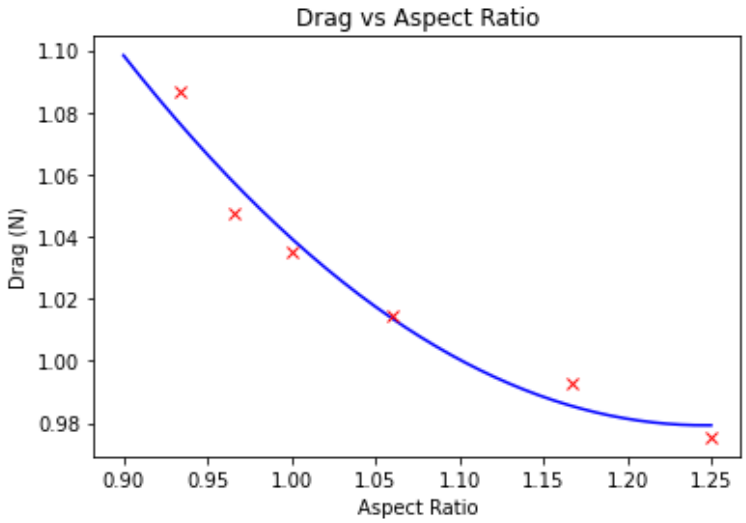

Figure 30: Aerodynamic Drag vs Dome Aspect Ratio

Plotting the resultant force (see Figure 30) results with the proposition that with an increasing aspect ratio (up to 1.25), the drag decreases. However, it must be noted that with increasing aspect ratio, the space within the central dome reduces, leaving less room for other components (mostly electronics). Therefore, an aspect ratio of **1.2** (width: 70mm and height: 58mm) is most suitable.

4.1.2. Optimized Airfoil Geometry and Configuration

As discussed in the previous chapter, twelve different prototypes were simulated to optimize for maximum thrust. Figure 31 shows velocity contour diagrams for four of the twelve prototypes. The contours are drawn at the symmetry plane of the air multiplier.

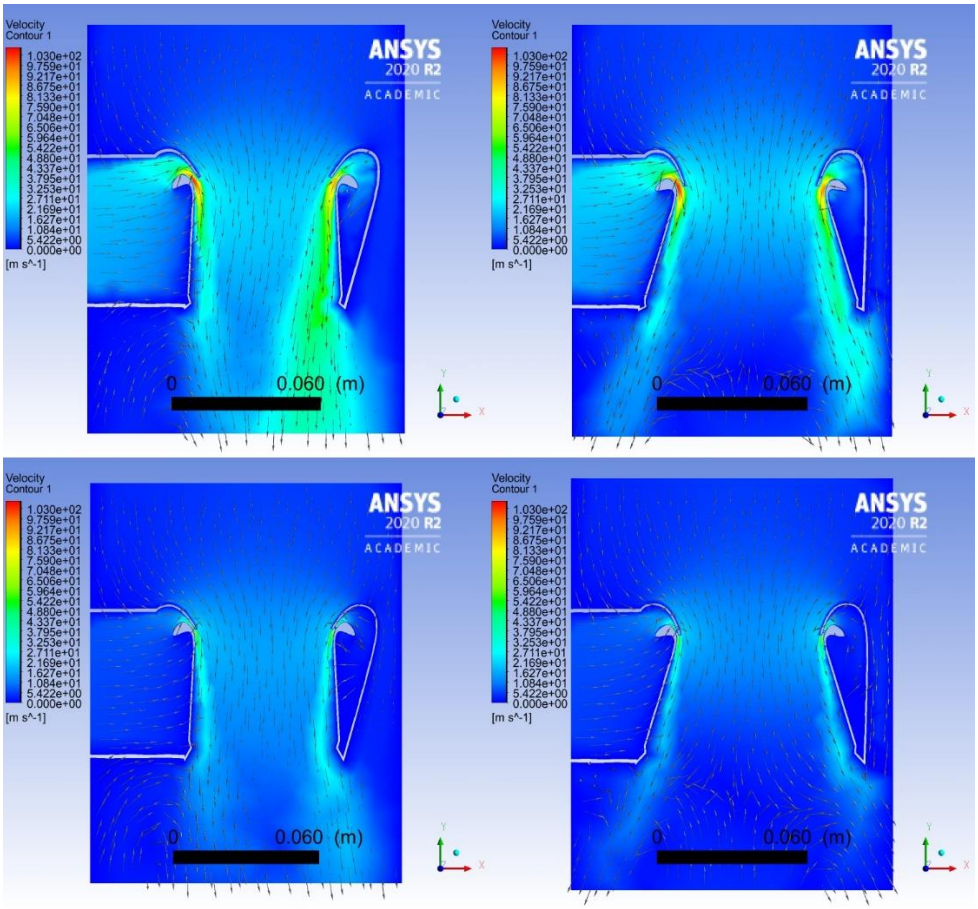

Figure 31: Velocity Contours for Flow Through Four Different Air Multipliers

The contours shown in Figure 31 are for (ordered from left to right followed by top to bottom) prototype 3 (wide) – 10°, prototype 3 – 0°, prototype 1 (narrow) – 10°, and prototype 1 – 0°.

Table 3 shown below summarizes the results. For the airfoil geometry with the highest thrust, the airfoil tilt angles are plotted in Figure 32 for more accurate results.

Table 3: Recorded Data for Airfoil Geometry and Configuration

Prototype No.	Tilt Angle °	No. of Mesh Elements	Lift N
1	0	483829	0.8855
1	7	491766	0.9921
1	10	487219	1.0260
1	14	487449	1.0981
2	0	485693	1.7380
2	7	494364	2.0020
2	10	487661	2.0580
2	14	487925	2.1550
3	0	507299	2.9580
3	7	491087	3.3550
3	10	499771	***3.3921***
3	14	491415	3.3290

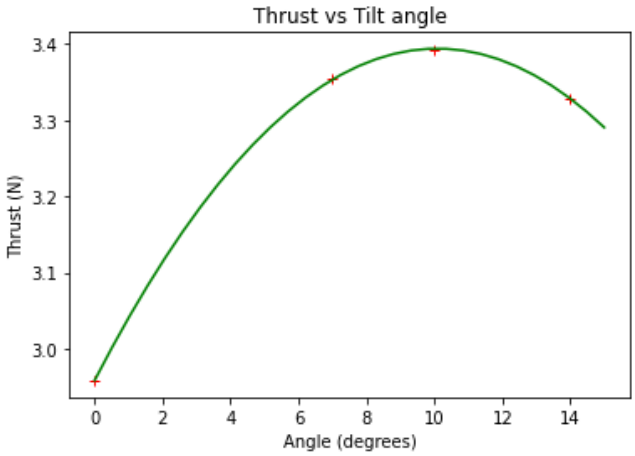

Figure 32: Thrust vs Airfoil Tilt Angle for Prototype 3

Prototype 3 has produced the greater thrust for all tilt angles. Moreover, an airfoil tilt angle of 10 degrees provided the greatest thrust, however, interestingly, this was not the case for other prototypes. Additionally, for prototype 3, the data for tilt angles would be plotted and an approximate quadratic equation would be fitted for optimized results. The optimal value for tilt is determined to be **10.1°**. The thrust for this tilt angle (with prototype 3) is **3.394 N**. This compared with the 4.75 N expected thrust for the fan alone (with 90% FSA) represent a 28.5% loss. However, the losses assumed by the fan alone are not entirely considered, making the loss estimate a conservative one.

4.1.3. Optimized Air Multiplier Diameter

For the diameter, air multipliers with several values of diameter (ranging from 40mm to 100mm) were optimized. For each of the diameters, three values were recorded: the mass of the air multiplier, the lift generated, and the velocity ratio for diametrically opposite nozzle points (inlet and farthest from inlet). Not only is the difference between lift and mass considered, but the diametrically opposite velocity ratio is also of prime importance. These values are recorded in Table 4. As discussed in previous chapters, the airflow through the nozzle of the air multiplier must be uniform. Non-uniform airflow will mean that not only will the thrust be generated at a point other than the center of the air multiplier toroid, but it will also be irregular with a change in inlet airflow. For control purposes, this

can increase uncertainties and also substantially increase the response time (time between changing motor speed and the change in airflow profile/thrust). Therefore, the difference between lift and mass is scaled by the ratio of velocities at opposite ends of the nozzle (this ratio is a kind of representation of uniformity of flow along the arc of the nozzle). The results are then plotted to determine optimum diameter (see Figure 34).

Table 4: Recorded Data for Air Multiplier Diameter

Diameter mm	No. of Mesh Elements	Lift (L) N	Mass (m) g	Velocity Ratio (V_R)	Resultant Parameter ($P_R = (L - mg) * V_R$) N
43.26	437966	2.7053	39.36	0.9579	2.2051
52.66	507947	2.8353	43.76	0.8993	2.1204
61.80	485361	3.1853	48.07	0.8766	***2.3205***
71.07	480723	3.3239	52.46	0.7610	2.0150
80.34	494841	3.4277	56.87	0.7001	1.8419
92.70	500643	3.5455	62.78	0.6692	1.7566

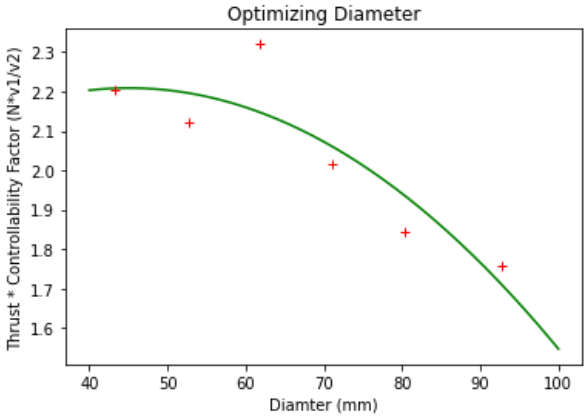

Figure 33: Resultant Parameter Value vs Air Multiplier Diameter

It can be noted that by increasing the diameter of the air multiplier, the lift increases. This was expected as was concluded in [35]. However, because of the disadvantages of a larger air multiplier about a system requiring predictable and quick responses, the results had to be scaled. From the results plotted in Figure 33, a diameter between **40mm and 50mm** is most suitable. Since the simulations for airfoil geometry and configuration were done with an air multiplier diameter within this range, a new simulation for final thrust is not required. Additionally, the velocity contours relevant to these simulations are similar to Figure 31 and hence not shown. Moreover, Appendix III shows the procedure to determine the velocity ratio considered in the simulations of this section.

4.2. Design Validation and Specifications

This section will focus on summarizing the optimizations achieved from the previous sections and combining them with design features to determine various constants that are essential to model control. Moreover, a simple check would be done to ensure that the maximum thrust achievable by the drone exceeds the weight of the drone with a suitable factor of safety. Finally, design specifications (mass, span, flight time, etc.) along with component costing are also a part of this section.

First of all, the constants discussed in section 3.3.1. will be determined from the optimum lift value obtained from simulations, and other geometric aspects of the design. The values for $K_S, K_C, \gamma, m, I_{XX}, I_{YY}, I_{ZZ}, and\ l$ would be determined while the values for $B_S, B_C, I_R, A_R, A_X, A_Y, A_Z$ would be assumed from either previous calculations or [40]. The fan specifications are taken from: [37] for side fans and [41] for the central fan. This will help determine the max RPMs (continuous and burst) that each fan can run at, which can give us an estimate of B (torque constant) for the fans. However, for this project, the values of the torque constant for both the fans are kept the same for the purpose of simplicity. . Also, it can be noted that the effect of torque by an EDF is minimum because of the presence of a stator after the rotor that straightens out the flow. Nevertheless, it is advisable to design fans in such a way that $B_C = 4B_S \sin\gamma$

Table 5: Final Parameter Values

Parameter	Value	Parameter	Value
m	1.502 kg	B_C	7.1582 e-11
l	0.223 m	B_S	7.1582 e-11
γ	15°	I_R	3.357 e-05 kg.m^2
I_{XX}	13.8 e-03 kg.m^2	A_R	0.20
I_{YY}	13.8 e-03 kg.m^2	A_x	0.30
I_{ZZ}	24.9 e-03 kg.m^2	A_y	0.30
K_C	5.2103 e-09	A_z	0.25
K_S	2.2282 e-09	-	-
$RPM_{max,C}$	43200	-	-
$RPM_{max,S}$	38600	-	-

Table 5 is a list of all of the parameters discussed in the previous paragraph alongside their values.

For the parameters with no unit, the unit can be derived from the corresponding equations in section 3.3.1. Following this, the design specifications for the drone are summarized. The final goal is to determine a FOS (which can be used to calculate payload capacity by setting a value for minimum FOS, which can vary according to use case) and flight time. Drone flight times are calculated based on using 3S LiPo batteries with a 5200mAh capacity. Table 6 records these results while Table 7 lists the components along with their costs. Moreover, comprehensive calculations arriving at these results can be found in Appendix IV.

Table 6: Design Specifications for Penta-copter

Design Specification	Value
Drone Mass	1.502 kg
Drone Span	500mm
Maximum Burst Thrust	2.510 kg
Maximum Continuous Thrust	2.321 kg
Factor of Safety (FOS)	**1.545**
Minimum Flight Time (65% throttle)	2.55 min
Average Flight Time (75% throttle)	**3.39 min**
Maximum Flight Time (100% throttle)	3.93 min

Table 7: Components List with Costing

Component	Cost (Rs.)
Structure (3D printing including material)	38,564 (Nylon + SLS) – 112,160 (ABS + FDM)
EDFs (1 central fan 64mm + 4 side fans ~47mm)	23,800
4 x Batteries (3S, 1300mAh, 35C)	6,000
Electronics (Controller, Receiver, ESCs, Sensors) + Misc. costs	16,500
Total	**84,864 – 158,460**

It must be noted that the cost for such a design is higher than what a conventional quadrotor would cost (with similar specifications); however, that fact can be attributed to the use of 3D printing as a manufacturing process. 3D printing is only feasible for prototype development, and the use of Nylon-11 with Selective Laser Sintering (SLS) can be significantly cheaper than the use of ABS-PC with Fused Deposition Modeling (FDM). For production purposes, an economical manufacturing process such as injection molding would be best suited.

4.3. Control Simulation

The flight controller block model used in this project is a derivative of the one used in the *Quadcopter Project* by MATLAB [42]. Figure 34 shows the block diagram for the flight controller. A total of six PD/PID controllers were used in this *Flight Controller* Simulink block.

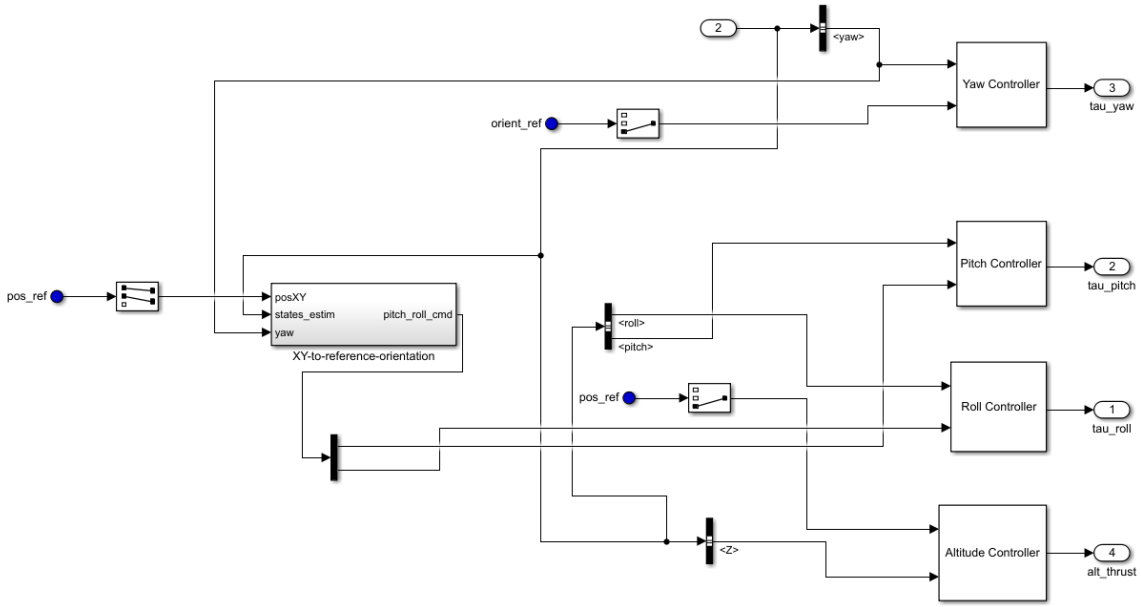

Figure 34: Flight Controller Block Diagram

The *XY-to-reference-orientation* (also used in [42]) block indirectly controls (using PD controllers) translation in the X and Y direction by changing the set point for pitch and roll, respectively. There are two controllers in this block. Additionally, four other controllers can independently control roll, pitch, yaw, and altitude. Internal block diagrams for controllers can be found in Appendix V. This section further records the tuned PD/PID parameters, using which motion through a trajectory is controlled.

4.3.1. Tuned Parameters for PD/PID Controllers

PD/PID controllers are tuned either by using the auto-tune method (feedback linearization) present in the control design toolbox of MATLAB, or manually. Auto-tune was used for the altitude controller and yaw controller, while the rest of the four controllers were manually tuned. Both the altitude and yaw controllers were PID, while the X → pitch, Y → roll, roll, and pitch controllers were PD. Table 8 shows the tuned parameters alongside remarks regarding miscellaneous setup (saturation at the output, variable K_p, etc.)

Table 8: Tuned PD/PID Controllers Parameters

Controller	K_p	K_d	K_i	Remarks
Altitude	12.4	4.22	8.23	Value of drone weight is added to the output
Yaw	0.359	0.243	0.0236	Output saturated dynamically (according to reference)
X → Pitch	0.0640	0.120	0	Output saturated to +/- 0.122
Y → Roll	-0.0640	0.120	0	Output saturated to +/- 0.122
Roll	0.04/ref.	0.05	0	K_p is variable (scaled by reference)
Pitch	0.04/ref.	0.05	0	K_p is variable (scaled by reference)

It is important to note that the output for the X/Y to Pitch/Roll controllers is in radians. Moreover, for the roll and pitch controllers, it was necessary to scale the proportional constant by the reference value to avoid large values for rotational speed that could potentially make the drone unstable.

4.3.2. Testing Controller on Example Trajectories

To test the tuned parameters from the previous sections, an example trajectory is employed. The attitude references have been set to a constant value (roll and pitch were set to 0° while yaw was set to 5°), while the position of the drone in the coordinate space is changed via signals comprising of step inputs. The signal editor tool for MATLAB is used for this purpose. Figure 35 shows the input signal for the X, Y, and Z positions of the drone, displayed in a scope (plot shown in Figure 35) that is fed data by the three signal editors. The vertical axis corresponds to the magnitude of the signal (in meters). A varying signal (30 seconds as signal time) with multiple waypoints is provided as input trajectory. This trajectory is then fed to the flight controller, within which X and Y are converted to appropriate pitch and roll response, and Z is fed to the altitude controller.

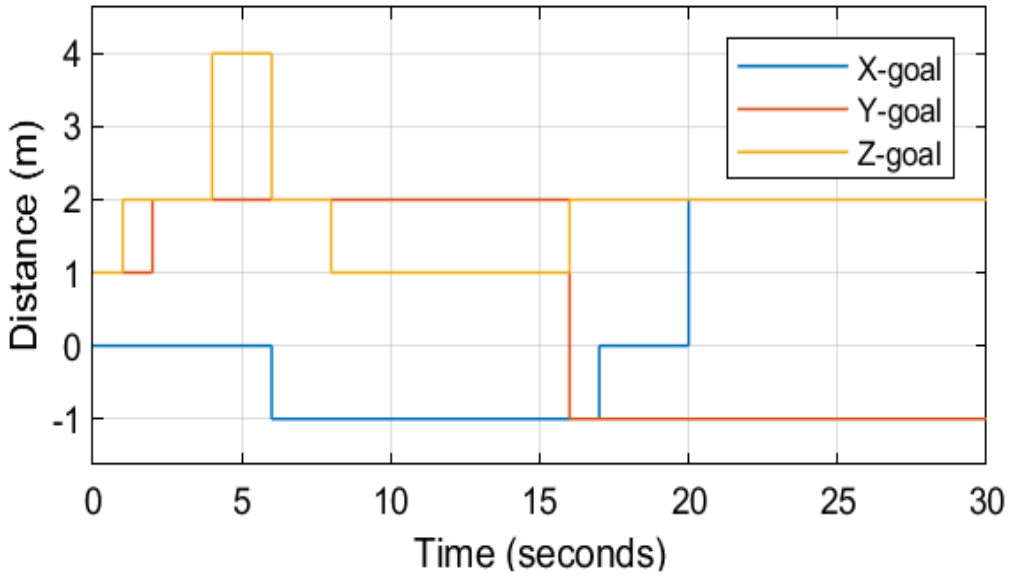

Figure 35: Signal Input for Position in Coordinate Space

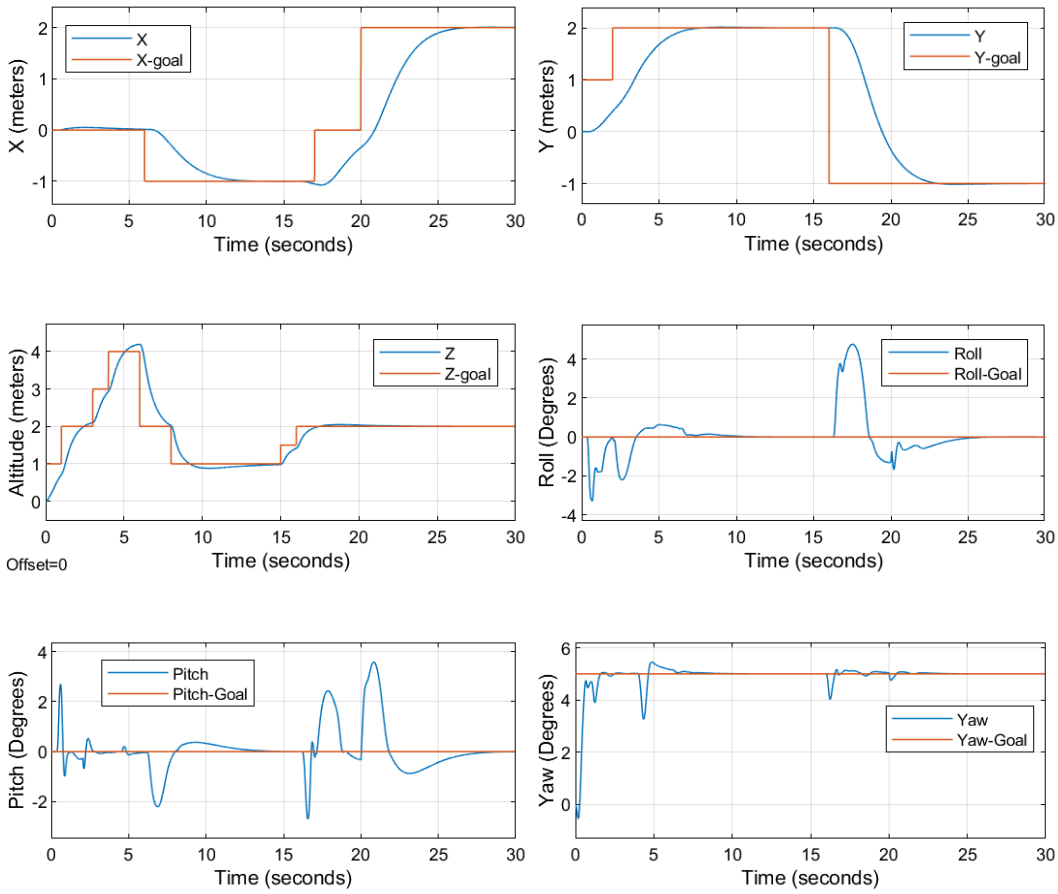

Figure 36: Position and Attitude Plots for the Drone

The actual and reference values for each of the six states of the drone (X, Y, Z, roll, pitch, and yaw) are attached to scopes to determine performance). Figure 36 shows these results.

These results prove that the controller can adequately control movement in 6 DOF. Moreover, there are a few findings to discuss. It can be noted that the response time for movement in the X and Y direction is high. This is expected because this time depends on the response of the pitch and roll controllers. The overshoot, in this case, is minimal which is highly desirable for movement in confined spaces. For the altitude, both the response time and overshoot are low. Furthermore, the roll and pitch variations remain within 5 degrees. This shows that the drone does not require substantial tilting to move in the lateral

plane, which is because the side arms are tilted. The yaw controller also has a suitable response with minor fluctuations.

Although the results shown in Figure 36 are acceptable, there are a few negatives to consider. The side arm tilt means that the drone has to tilt less for more lateral movement, however, this also means that wind effects can be more significant for such a design. Moreover, large yaw movements have also shown to unbalance the drone, and as such gradual yawing movement is advised (a ramp signal with low gradient). All things considered, the controllers with tuned parameters discussed earlier have shown more than satisfactory performance in point-to-point movement in 3D space which is proof for the controllability of this design.

Additionally, Figure 37 displays the actual trajectory of the drone in 3D space for two different trajectory inputs. Input trajectories are in the form of waypoints (coordinates in 3D space) at specific time periods (for rapid changes in X and Y, suitable time is set so that the drone reaches the waypoint, with a total simulation time of 30 seconds). Moreover, for these simulations, the yaw reference is set to zero.

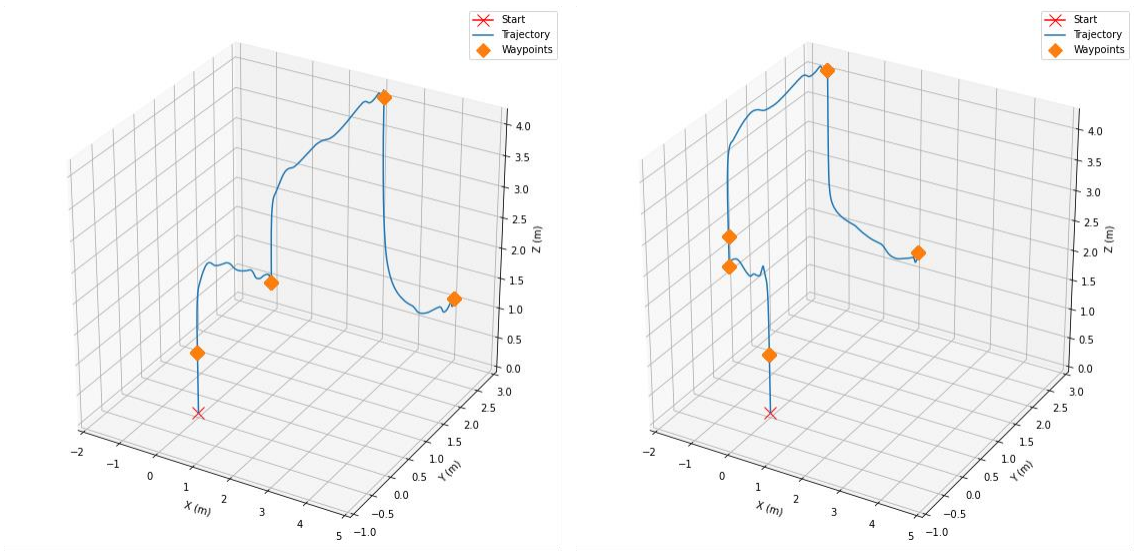

Figure 37: Drone Trajectory in 3D Plots

CHAPTER 5: CONCLUSION AND RECOMMENDATION

We have proposed a bladeless drone design that is considerably safer than conventional propeller-based drones. This design successfully conceals bladed components of propulsion devices with satisfactory losses. This chapter includes a summary of the results and findings of this project along with recommendations for future research.

5.1. Summary of Results

The bladeless drone design comprising of a central dome (housing a fan) with four side arms (each also housing a fan). The central dome aspect ratio was optimized for minimum drag and mass. An aspect ratio of 1.2 was found to be most suitable as it provided lower drag while leaving enough volume in the central dome to house miscellaneous equipment and electronics. The air multiplier was also optimized for maximum thrust and minimum mass. This optimization was divided into two categories: airfoil geometry and configuration, and air multiplier diameter. Three prototypes for the airfoil geometry were analyzed, and it was concluded that the prototype with the widest nozzle proved to be the most effective. Furthermore, for this prototype, an airfoil tilt angle of 10 degrees was best. For the air multiplier diameter, similar CFD simulations were run to conclude that a diameter between 40mm and 50mm was most suitable.

For the resulting optimized geometry, the design was validated by both comparing its thrust output to its weight and designing a controller to verify controllability in 3D space. The drone with a span of 50 cm weighed approximately 1.5 kg with a continuous thrust capability equivalent to approximately 2.3 kg, resulting in a factor of safety of 1.545 without payload. This value for the FOS is decent as it not only allows for some payload but also caters to the gradual wear of the motors. It was also concluded that the drone can fly for about 2.5 to 3.4 minutes with a 5200 mAh battery.

Finally, for the control simulation, six PD/PID controllers with tuned parameters were effectively able to navigate the drone through a complex trajectory (point-to-point

movement in 3D space). Not only did this prove the controllability of the drone, but it also revealed salient features of the drone which include the following. Owing to the side arm tilt, the drone requires less tilting to achieve the same lateral movement, when compared with a conventional drone with straight arms. Moreover, the drone response for movement in the X and Y direction exhibited very little overshoot (but with a high response time). This is essential as the drone is targeted for use in confined spaces and overshoots are not desirable. The rest of the controllers have decent response times and overshoot.

All of these results validate the drone design and utility, which coupled with increased safety make it a good choice for flights in crowded spaces/areas. However, it is important to note that the drone is less efficient than a conventional propeller-based drone owing to the losses with regards to airflow through the air multiplier (inducement does not completely offset these losses, however, the difference gradually decreases with an increase in inducement if the size of air multiplier is increased), and as such is advised for use cases demanding safety.

5.2. Future Work

Fabricating a prototype based on optimized geometry is of paramount importance. The results need to be validated in the real environment before giving a final verdict on the feasibility of this design. The optimizations discussed in this report provide a decent start and greatly help reduce the number of prototypes required to perfect the design.

Furthermore, the scalability of such a design needs to be evaluated. We have discussed the caveats associated with a large diameter for the air multiplier (about its predictability in control modeling). A relationship between the resultant position of the thrust (within the air multiplier loop) and the shape and configuration of the air multiplier needs to be determined. Such a relationship can then be incorporated into the plant model. This is necessary because a larger air multiplier produces more thrust due to inducement which would be preferable for larger variations of this design for improved payload capacity and

more complex tasks. In addition to this, an additional structure for payload also needs to be designed.

Furthermore, one important line of research could be the use of propulsion devices other than EDFs. This may include, but are not limited to, centrifugal compressors and gas turbines, with the latter being more feasible for larger variations of the drone. Moreover, work also needs to be done to investigate the effect of vents and meshes (present in protective covers) in the airflow and subsequently the efficiency of the propulsion device.

Finally, work can be done on using controllers other than PID, that can be used for such nonlinear systems with better transient responses. Moreover, environmental effects and the use of sensor feedback also need to be explored in the control system design.

REFERENCES

[1] The Drone Market Report 2020-2025. Retrieved from: https://www.researchandmarkets.com/reports/5117908/the-drone-market-report-2020-2025

[2] Yoganandan, N., et al., Biomechanics of skull fracture. 1995. 12(4): p. 659-668.

[3] Moskowitz, E.E., et al., Aerial drone misadventure: A novel case of trauma resulting in ocular globe rupture. 2018. 10: p. 35-37.

[4] Crahay, François-Xavier, R. Rampat, M. Tonglet and J. Rakic. “Drones’ side effect: facial and ocular trauma caused by an aerial drone.” BMJ Case Reports 14 (2021): n. pag.

[5] Johnson, J., Megan R Svach and L. Brown. “Drone and Other Hobbyist Aircraft Injuries Seen in U.S. Emergency Departments, 2010-2017.” American journal of preventive medicine 57 6 (2019): 826-829.

[6] Cauchard, Jessica R., Jane L. E, Kevin Y. Zhai, and James A. Landay. "Drone & me: an exploration into natural human-drone interaction." In Proceedings of the 2015 ACM international joint conference on pervasive and ubiquitous computing, pp. 361-365. 2015.

[7] Duncan, Brittany A., and Robin R. Murphy. "Comfortable approach distance with small unmanned aerial vehicles." In 2013 IEEE RO-MAN, pp. 786-792. IEEE, 2013.

[8] Use of drones, flying cameras banned in Punjab. Retrieved from: https://www.dawn.com/news/1489009.

[9] Tritton, D.J., Physical Fluid Dynamics, Van Nostrand Reinhold, 1977 (reprinted 1980), Section 22.7, The Coandă Effect.

[10] Reba, Imants. "Applications of the Coanda effect." Scientific American 214, no. 6 (1966): 84-93.

[11] Das, S., M. Abdollahzadeh, J. Pascoa, A. Dumas, and M. Trancossi. "Numerical modeling of coanda effect in a novel propulsive system." The International Journal of Multiphysics 8, no. 2 (2014): 181-202.

[12] Bharathwaj, R., P. Giridharan, K. Karthick, C. Hari Prasath, and K. Prakash Marimuthu. "Computational study of Coanda based Fluidic Thrust Vectoring system for optimising Coanda geometry." In IOP Conference Series: Materials Science and Engineering, vol. 149, no. 1, p. 012210. IOP Publishing, 2016.

[13] Han, Seonhye, Hyunyong Lee, Hyoju Lee, Jaehyeok Jeon, Choonghan Lee, Yong Bum Kim, and Hyouk Ryeol Choi. "A flying saucer lifted with Coandă effect." In 2014 IEEE International Conference on Robotics and Automation (ICRA), pp. 2561-2561. IEEE, 2014.

[14] Geoffrey Hatton, “GFS Project Ltd., Thrust Generation”, UK Patent Office no. GB 2,242,406/23.03.2005.

[15] Aabid, Abdul, and S. A. Khan. "Design and Fabrication of Flying Saucer Utilizing Coanda Effect." In IOP Conference Series: Materials Science and Engineering, vol. 370, no. 1, p. 012060. IOP Publishing, 2018.

[16] Haque, Md Enamul, Mohammad Mashud, and Md Nazmul Hasan. "Unmanned Aerial Vehicles Construction by Coandă Effect." ICERIE (2017).

[17] Djojodihardjo, Harijono, Riyadh Ibraheem Ahmed, and Ali Yousefian. "An analysis on the lift generation for Coandă micro air vehicles." In 2014 IEEE International Conference on Aerospace Electronics and Remote Sensing Technology, pp. 164-169. IEEE, 2014.

[18] Lee, Hyunyong, Seonhye Han, Hyoju Lee, Jaehyeok Jeon, Choonghan Lee, Yong Bum Kim, Seung Hwan Song, and Hyouk Ryeol Choi. "Design optimization, modeling, and control of unmanned aerial vehicle lifted by Coandă effect." IEEE/ASME Transactions on Mechatronics 22, no. 3 (2017): 1327-1336.

[19] Shin, Dongyoon, Hyeji Kim, Jihyuk Gong, Uijeong Jeong, Yeeun Jo, and Eric Matson. "Stealth UAV through Coanda Effect." arXiv preprint arXiv:2005.14629 (2020).

[20] Tello | Ryze Tech - Feel the Fun. Retrieved from: https://store.dji.com/product/tello?vid=45701&from=menu_products

[21] Joachims, Wim & de Bouw, Michael & Dubois, Samuel. (2020). Drones als hulpmiddel: Inzichten in nieuwe werkprocessen op de bouwwerf. 10.13140/RG.2.2.34515.73765.

[22] Dyson, James, and Peter David Gammack. "Fan." U.S. Patent Application 29/336,687, filed April 20, 2010.

[23] Nilesh Gandhi, “Propeller-less Drone Concept”. Retrieved from:

https://edu.3ds.com/en/projects/propellerless-drone-concept

[24] Jafari, Mohammad, Hossein Afshin, Bijan Farhanieh, and Atta Sojoudi. "Numerical investigation of geometric parameter effects on the aerodynamic performance of a Bladeless fan." Alexandria Engineering Journal 55, no. 1 (2016): 223-233.

[25] Jia, Muye. "Drone with no external propeller blades." U.S. Patent 10,336,452, issued July 2, 2019.

[26] Capunay, Austin, Daniel Valdenegro, Daniel A. GONZALEZ MASSO, and Luis Rodolfo GARCIA CARRILLO. "Bladeless unmanned aerial vehicle." U.S. Patent Application 16/007,854, filed May 2, 2019.

[27] Valdenegro, Daniel, Austin Capunay, Daniel Gonzalez, Luis Rodolfo Garcia Carrillo, and Pablo Rangel. "Improving Safety: Design and Development of a Bladeless Thruster for Autonomous Multi-copters." In 2018 International Conference on Unmanned Aircraft Systems (ICUAS), pp. 158-167. IEEE, 2018.

[28] Herrera Bladeless Drone, Uncrate. Retrieved from: https://uncrate.com/herrera-bladeless-drone/

[29] Yamada, Wataru, Hiroyuki Manabe, and Daizo Ikeda. "Zerone: Safety drone with blade-free propulsion." In Proceedings of the 2019 CHI Conference on Human Factors in Computing Systems, pp. 1-8. 2019.

[30] Jae-Sung, Moon, Choonghyun Kim, Youngil Youm, and Joonbum Bae. "UNI-Copter: A portable single-rotor-powered spherical unmanned aerial vehicle (UAV) with an easy-

to-assemble and flexible structure." Journal of Mechanical Science and Technology 32, no. 5 (2018): 2289-2298.

[31] Hover Camera Passport – Zero Zero Robotics. Retrieved from: https://zerozero.tech/hover-camera-passport?d=pc

[32] Fleye Ducted Fan Drone on Kickstarter. Retrieved from: https://www.youtube.com/watch?v=B9EY_cMx_7Q

[33] Jafari, M., H. Afshin, B. Farhanieh, and H. Bozorgasareh. "Numerical aerodynamic evaluation and noise investigation of a bladeless fan." Journal of Applied Fluid Mechanics 8, no. 1 (2015): 133-142.

[34] Jeong, Siyoung, Jongsoo Lee, and Jaehyun Yoon. "Optimal Nozzle Design of Bladeless Fan Using Design of Experiments." Transactions of the Korean Society of Mechanical Engineers A 41, no. 8 (2017): 711-719.

[35] Jafari, Mohammad, Hossein Afshin, Bijan Farhanieh, and Atta Sojoudi. "Numerical investigation of geometric parameter effects on the aerodynamic performance of a Bladeless fan." Alexandria Engineering Journal 55, no. 1 (2016): 223-233.

[36] Singh, Mohit, and Rupinder Singh. "Twin Screw Extrusion for Recycling of Thermoplastics." (2020)

[37] Great Planes Model Manufacturing Company & Electrify, Hyperflow Electric Ducted Fan Instruction Manual. Retrieved from: https://www.little-bellanca.com/manual_download/hyperflow370-manual-v1_1.pdf.

[38] Trancossi, Michele, and Mauro Madonia. The efficiency of an electric turbofan vs. inlet area: a simple mathematical model and CFD simulations. No. 2012-01-2217. SAE Technical Paper, 2012.

[39] Mahony, Robert, Vijay Kumar, and Peter Corke. "Multirotor aerial vehicles: Modeling, estimation, and control of quadrotor." IEEE robotics & automation magazine 19.3 (2012): 20-32.

[40] Suresh, H., Sulficar, A. and Desai, V. (2018) ‘Hovering control of a quadcopter using linear and nonlinear techniques’, Int. J. Mechatronics and Automation, Vol. 6, Nos. 2/3, pp.120–129.

[41] Powerfun EDF 64mm 11 Blades Ducted Fan with 3900KV 3S RC Brushless Motor Balance Tested for EDF 3S RC Jet Airplane. Retrieved from: https://www.amazon.com/Ducted-Blades-Brushless-3900KV-Airplane/dp/B07C3R2VB1

[42] The Quadcopter Project. Retrieved from https://www.mathworks.com/help/aeroblks/quadcopter-project.html

APPENDIX I: PENTA-COPTER PLANT MODEL

Similar to the control theory established in earlier sections, this code is also an extension of the MATLAB level 2 S-function used in [40]. The extension includes considerations for the penta-copter proposed in this project. The code structure is taken from [40] and is attributed as such.

```
function pentaplant(block)
setup(block);
function setup(block)
 block.NumInputPorts = 5;
 block.NumOutputPorts = 12;

 for i = 1:5
 block.InputPort(i).Dimensions = 1;
 block.InputPort(i).DirectFeedthrough = false;
 block.InputPort(i).SamplingMode = 'Sample';
 end
 for i = 1:12
 block.OutputPort(i).Dimensions = 1;
 block.OutputPort(i).SamplingMode = 'Sample';
 end

 block.NumDialogPrms = 0;
 block.NumContStates = 12;
 block.SampleTimes = [0,  0];
 block.SetAccelRunOnTLC(false);
 block.SimStateCompliance = 'DefaultSimState';
 block.RegBlockMethod('InitializeConditions', @InitializeConditions);
 block.RegBlockMethod('Outputs', @Outputs);
 block.RegBlockMethod('Derivatives', @Derivatives);
 block.RegBlockMethod('Terminate', @Terminate);

function InitializeConditions(block)
P=0; Q=0; R=0; Phi=0; The=0; Psi=0;
U=0; V=0; W=0; X=0; Y=0; Z=0;
init = [P,Q,R,Phi,The,Psi,U,V,W,X,Y,Z];
for i=1:12
block.OutputPort(i).Data = init(i);
block.ContStates.Data(i) = init(i);
end
function Outputs(block)
for i = 1:12
 block.OutputPort(i).Data = block.ContStates.Data(i);
end
function Derivatives(block)
P = block.ContStates.Data(1);
Q = block.ContStates.Data(2);
R = block.ContStates.Data(3);
phi = block.ContStates.Data(4);
```

```
theta = block.ContStates.Data(5);
psi = block.ContStates.Data(6);
U = block.ContStates.Data(7);
V = block.ContStates.Data(8);
W = block.ContStates.Data(9);
X = block.ContStates.Data(10);
Y = block.ContStates.Data(11);
Z = block.ContStates.Data(12);
w1 = block.InputPort(1).Data;
w2 = block.InputPort(2).Data;
w3 = block.InputPort(3).Data;
w4 = block.InputPort(4).Data;
w5 = block.InputPort(5).Data;

m=1.48; Ixx=13.8e-03; Izz=24.9e-03; Iyy=13.8e-03; Ir=3.357e-5; Ax=0.3;
Ay=0.3; Az=0.25; Ar=0.2;
rot_x = w1*0.966 - w3*0.966;
rot_y = w2*0.966 - w4*0.966;
rot_z = w1*0.259 + w2*0.259 + w3*0.259 + w4*0.259 - w5;
T_x = -5.767e-10*(w1^2) + 5.767e-10*(w3^2);
T_y = 5.767e-10*(w2^2) - 5.767e-10*(w4^2);
T_z = 2.1523e-09*(w1^2) + 2.1523e-09*(w2^2) + 2.1523e-09*(w3^2) +
2.1523e-09*(w4^2) + 5.2103e-09*(w5^2);
Mphi = -6.9143e-11*(w1^2) + 3.3423e-10*(w2^2) + 6.9143e-11*(w3^2) -
3.3423e-10*(w4^2);
Mthe = -3.3423e-10*(w1^2) - 6.9143e-11*(w2^2) + 3.3423e-10*(w3^2) +
6.9143e-11*(w4^2);
Mpsi = 1.8527e-11*(w1^2) + 1.8527e-11*(w2^2) + 1.8527e-11*(w3^2) +
1.8527e-11*(w4^2) - 7.7582e-11*(w5^2);
dU = (cos(psi)*cos(theta))*T_x/m + (cos(psi)*sin(theta)*sin(phi)-
sin(psi)*cos(phi))*T_y/m + (cos(psi)*sin(theta)*cos(phi) +
sin(psi)*sin(phi))*T_z/m - Ax*U/m;
dV = (sin(psi)*cos(theta))*T_x/m +
(sin(psi)*sin(theta)*sin(phi)+cos(psi)*cos(phi))*T_y/m +
(sin(psi)*sin(theta)*cos(phi) - cos(psi)*sin(phi))*T_z/m - Ay*V/m;
dW = -9.81 - sin(theta)*T_x/m + cos(theta)*sin(phi)*T_y/m +
cos(theta)*cos(phi)*T_z/m - Az*W/m;
dP= ((Iyy-Izz)/Ixx)*Q*R - (Ir/Ixx)*(Q * rot_z - R * rot_y) + Mphi/Ixx -
Ar*P/Ixx;
dQ= ((Izz-Ixx)/Iyy)*P*R - (Ir/Iyy)*(P * rot_z - R * rot_x) + Mthe/Iyy -
Ar*Q/Iyy;
dR= ((Ixx-Iyy)/Izz)*P*Q - (Ir/Izz)*(P * rot_y - Q * rot_x) + Mpsi/Izz -
Ar*R/Izz;
dPhi = P + sin(phi)*tan(theta)*Q + cos(phi)*tan(theta)*R;
dTheta = cos(phi)*Q - sin(phi)*R;
dPsi = sin(phi)/cos(theta)*Q + cos(phi)/cos(theta)*R;
dX = U;
dY = V;
dZ = W;
f = [dP dQ dR dPhi dTheta dPsi dU dV dW dX dY dZ].';

block.Derivatives.Data = double(f);
function Terminate(~)
```

APPENDIX II: MOTOR MIXING ALGORITHM

```
function [w1, w2, w3, w4, w5] = motor_mixing_algorithm(m_phi, m_theta, m_psi,
T)

w1 = 7.3605e+07*T - 3.1659e+09*m_phi + 4.9432e+09*m_psi + 1.8573e+09*m_theta;
w2 = 7.3605e+07*T + 4.3037e+09*m_phi + 4.9432e+09*m_psi - 3.5887e+09*m_theta;
w3 = 7.3605e+07*T - 2.5724e+09*m_phi + 4.9432e+09*m_psi + 4.7265e+09*m_theta;
w4 = 7.3605e+07*T + 1.4346e+09*m_phi + 4.9432e+09*m_psi - 2.9951e+09*m_theta;
w5 = 7.0308e+07*T - 8.1678e+09*m_psi;

limit = 38600;

if (w1 > 0)
    w1 = sqrt(w1);
    if (w1 > limit)
        w1 = double(limit);
    end
else
    w1 = double(0);
end

if (w2 > 0)
    w2 = sqrt(w2);
    if (w2 > limit)
        w2 = double(limit);
    end
else
    w2 = double(0);
end
if (w3 > 0)
    w3 = sqrt(w3);
    if (w3 > limit)
        w3 = double(limit);
    end
else
    w3 = double(0);
end
if (w4 > 0)
    w4 = sqrt(w4);
    if (w4 > limit)
        w4 = double(limit);
    end
else
    w4 = double(0);
end
if (w5 > 0)
    w5 = sqrt(w5);
    if (w5 > 43200)
        w5 = double(43200);
    end
else
    w5 = double(0);
end
end
```

APPENDIX III: VELOCITY RATIO FOR AIR MULTIPLIERS

To determine velocity ratios, the velocity at the symmetry plane is plotted. The maximum velocity at each end of the air multiplier nozzle is shown as *peaks* for each air multiplier diameter, which can then be extracted by exporting the chart data. Dividing these maximum velocities results in the velocity ratio that is utilized in Table 4. Figure 38 shows the plot.

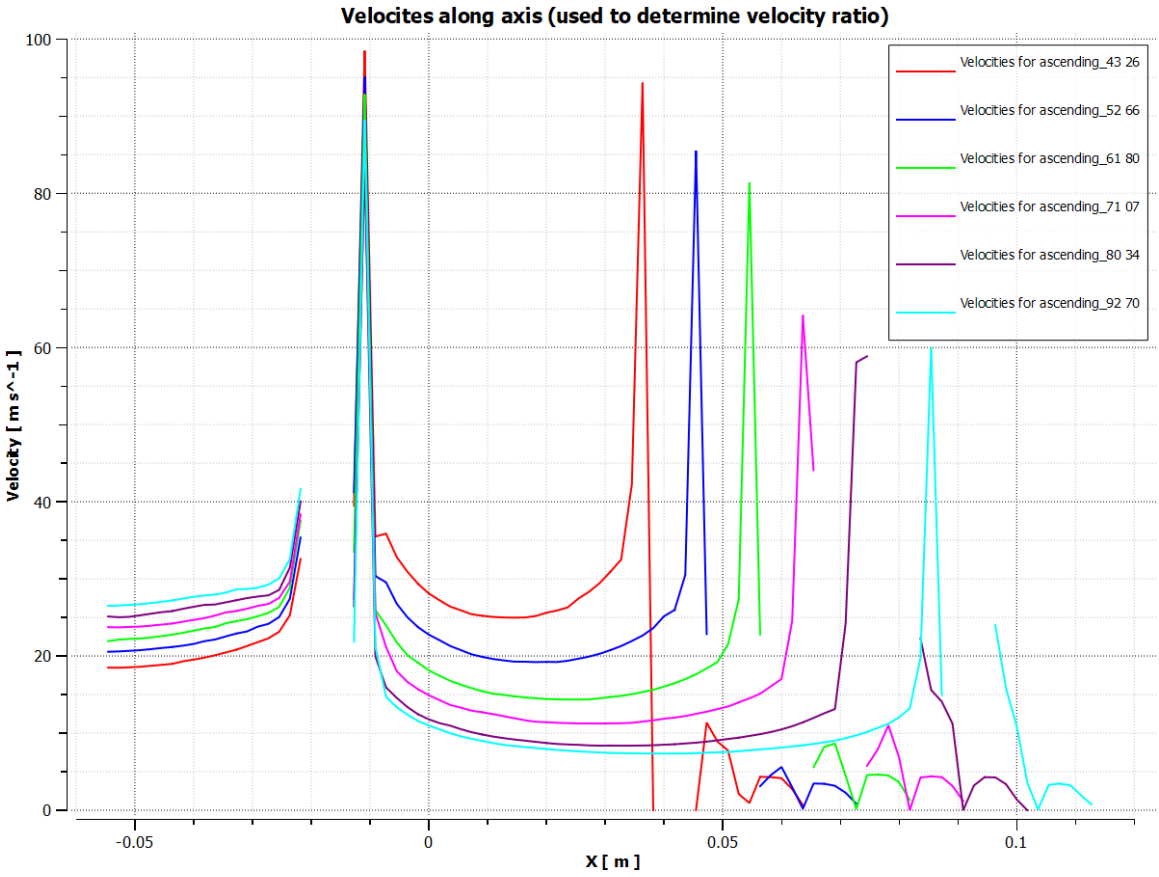

Figure 38: Velocity Plot for Velocity Ratios

APPENDIX IV: CALCULATIONS FOR DESIGN VALIDATION

$upper\_half\_mass := 65.50\ gm$
$lower\_half\_mass := 54.08\ gm$
$central\_body\_mass := upper\_half\_mass + lower\_half\_mass = 119.58\ gm$
$central\_fan\_mass := 150\ gm$
$thruster\_structure\_mass := 60.70\ gm$
$thruster\_fan\_mass := 138\ gm$
$single\_battery\_mass := 102\ gm$
$single\_thruster\_total\_mass := thruster\_structure\_mass + thruster\_fan\_mass + single\_battery\_mass = 300.7\ gm$
$misc\_equipment\_mass := 30\ gm$

$Total\_mass := central\_body\_mass + central\_fan\_mass + 4 \cdot single\_thruster\_total\_mass + misc\_equipment\_mass = 1.502\ kg$

$battery\_voltage := 11.1\ V$
$single\_battery\_capacity := 1300\ mA \cdot hr$
$total\_battery\_capacity := 4 \cdot single\_battery\_capacity = 5.2\ A \cdot hr$

$arm\_fan\_dia := 47.2\ mm$
$central\_fan\_dia := 64\ mm$

$ueptf := 221\ W \quad meptf := 221\ W$
$uepcf := 550\ W \quad mepcf := 655\ W$

$forw\_factor\_nozzle := 0.71 \cdot \frac{ueptf}{meptf} = 0.71$

$max\_rpm\_side := 38600\ rpm = (4.042 \cdot 10^3)\ \frac{1}{s}$

$theor\_thrust\_arm\_fan := 485\ gm$

$max\_rpm\_central := 43200\ rpm = (4.524 \cdot 10^3)\ \frac{1}{s}$

$forw\_factor\_central := \frac{uepcf}{mepcf} = 0.84$

$max\_electrical\_current\_thruster\_fan := 19.9\ A$
$max\_electrical\_current\_central\_fan := 52\ A$

$theor\_thrust\_central\_fan := 1180\ gm$

$thruster\_tilt\_angle := 15\ °$

$max\_thrust\_arm\_fan := forw\_factor\_nozzle \cdot theor\_thrust\_arm\_fan \cdot \cos(thruster\_tilt\_angle) = 332.617\ gm$
$max\_thrust\_central\_fan := forw\_factor\_central \cdot theor\_thrust\_central\_fan = 990.84\ gm$
$power\_consumption\_max := uepcf + 4 \cdot ueptf = (1.434 \cdot 10^3)\ W$

$capacity := 5.2\ A \cdot hr \cdot 11.7\ V \cdot 60\ \frac{min}{hr} = (3.65 \cdot 10^3)\ W \cdot min$

$min\_time := \frac{capacity}{power\_consumption\_max} = 2.546\ min$

$Max\_combined\_thrust := max\_thrust\_central\_fan + 4 \cdot max\_thrust\_arm\_fan = 2.321\ kg$

$Surplus\_thrust := Max\_combined\_thrust - Total\_mass = 818.926\ gm$

$moderate\_power := \frac{Total\_mass}{Max\_combined\_thrust} \cdot power\_consumption\_max = 928.104\ W$

$moderate\_time := \frac{capacity}{moderate\_power} = 3.933\ min$

Figure 39: Design Validation Calculations

APPENDIX V: PENTA-COPTER SIMULINK BLOCK DIAGRAMS

Figure 27 shows the complete (highest level) block diagram for the Simulink system. This consists of a flight controller (shown in Figure 34), a MATLAB function for motor mixing algorithm (see Appendix II), a level 2 S-function for pentacopter model (see Appendix I), a block for Simulink 3D simulation, and a reference and state block which generates the reference trajectory and feeds that (along with feedback states) to the flight controller. The flight controller consists of multiple controllers which are shown in the following order in Figure 40: altitude, roll, pitch, yaw.

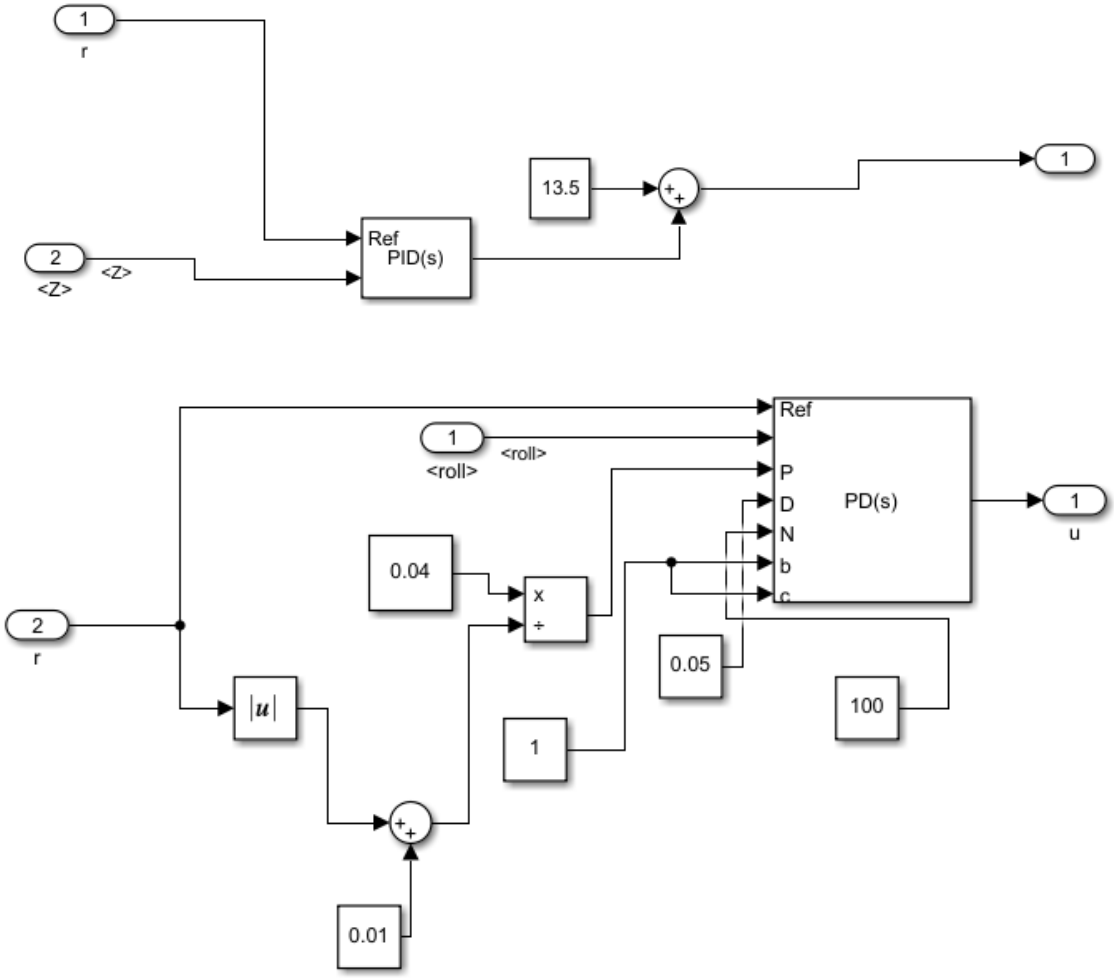

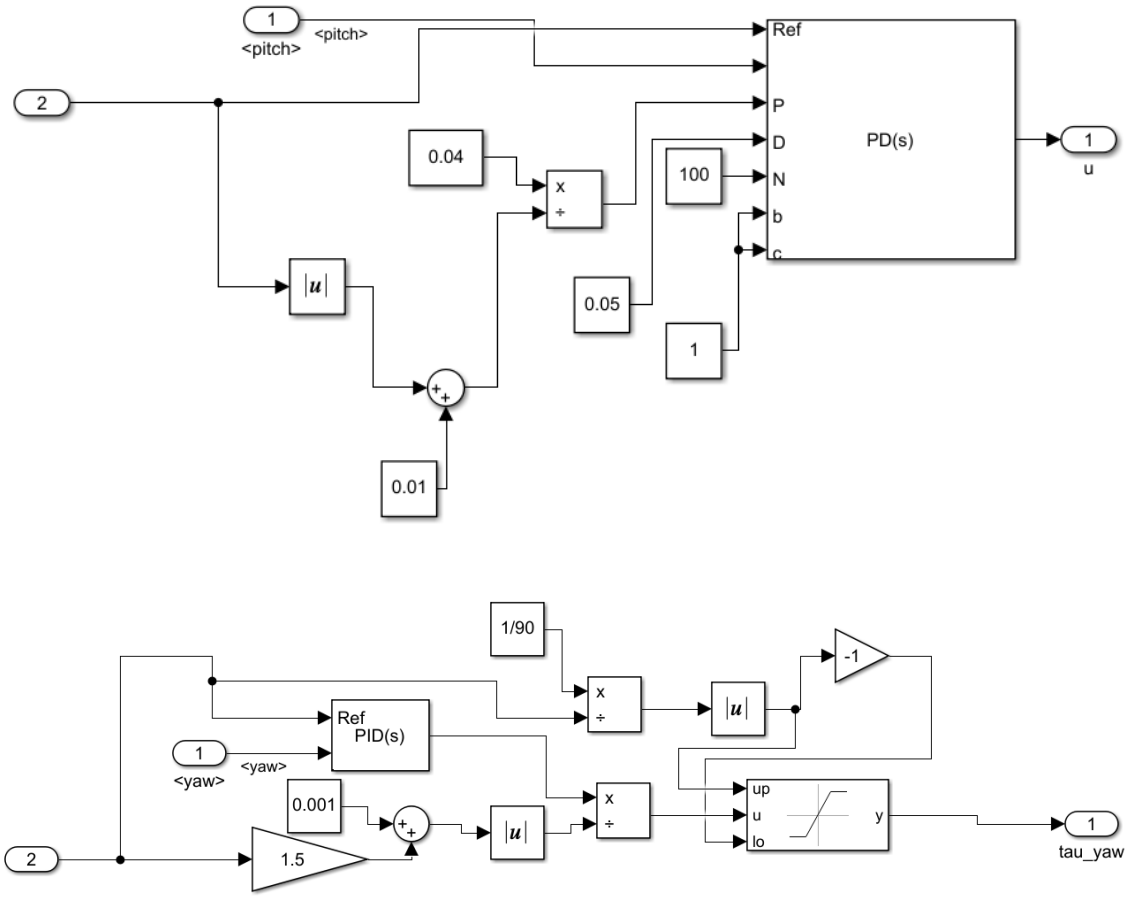

Figure 40: Block Diagrams for Controllers (Altitude, Roll, Pitch, and Yaw)